Åsmund Aamodt Resell

Intracranial Pulsatility

A Novel Computational MPET Framework
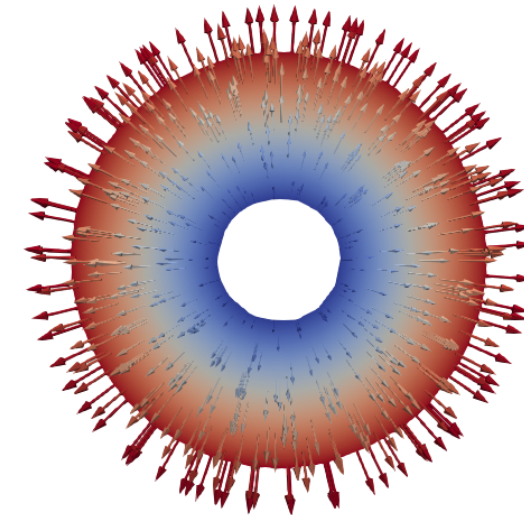
June 2022

Master's thesis

Master's thesis

2022

Åsmund Aamodt Resell

NTNU
Norwegian University of
Science and Technology

NTNU
Norwegian University of
Science and Technology

Intracranial Pulsatility

A Novel Computational MPET Framework

Åsmund Aamodt Resell

Department of Structural Engineering
Faculty of Engineering
NTNU - Norwegian University of Science and Technology

MASTER THESIS 2022

SUBJECT AREA: Biomechanics	DATE: 11.06.2022	NO. OF PAGES: 62

TITLE:

Intracranial Pulsatility - A Novel Computational MPET Framework

Pulsatilitet i kraniet – Et nytt rammerverk for MPET beregninger

BY:

Åsmund Aamodt Resell

SUMMARY:
The brain can be considered a porous medium permeated by different types of fluid, most notably: blood, interstitial fluid (ISF) and cerebrospinal fluid (CSF). In recent years, models based on multiple-network poroelasticity theory (MPET) have seen an increased popularity for studying the brain. Although some of these studies using MPET models have included the effect of the cardiac cycle through cerebral pulsatile blood flow, no previous study has related cardiac-induced intracranial pulsatility to clinical measurements of pressure, displacements, and flow rates with both mean values and pulsatile amplitudes in mind. Whats more, all previous MPET studies have fixed the displacement on the cortical surface, which is a crude approximation, as the pulsatile variation in intracranial pressure (ICP) has been shown to depend heavily on the expansion and contraction of brain tissue.

 In this thesis, a novel method to model intracranial pulsatility is introduced. The method includes a three-network MPET model of the brain, coupled with a compartment model that represents ICP in the subarachnoid space (SAS) and in the cerebral ventricles. The compartment model is non-linear due to the exponential intracranial pressure-volume relation caused by the rigid confines of the skull. Furthermore, traction boundary conditions are used on the brain surfaces instead of fixed displacements, which allows for the motion of brain tissue along with net CSF exchange to directly drive the pulsatile pressures of the compartment model. The poroelastic domain of the brain is solved using the finite element framework FEniCS, with an implicit Euler scheme in time.

The results of the proposed model are compared and discussed with clinical measurements of pulsatility. The pressure characteristics of the numerical results agree well with clinical data in all three fluid networks and in the compartment model. Displacements and flow rates are also in good agreement with several clinical indicators. This thesis demonstrates the possibility of recreating a realistic relation between pressure, deformation, and fluid flow using the proposed model. The thesis also illustrates that modeling pulsatility with MPET models requires a component that accounts for the non-linear relation between brain expansion, CSF flow, and ICP.

RESPONSIBLE TEACHER: Victorien Prot

SUPERVISOR(S) Victorien Prot

CARRIED OUT AT: Department of Structural Engineering, NTNU and Simula Research
Laboratory

Abstract

The brain can be considered a porous medium permeated by different types of fluid, most notably: blood, interstitial fluid (ISF) and cerebrospinal fluid (CSF). In recent years, models based on multiple-network poroelasticity theory (MPET) have seen an increased popularity for studying the brain. Although some of these studies using MPET models have included the effect of the cardiac cycle through cerebral pulsatile blood flow, no previous study has related cardiac-induced intracranial pulsatility to clinical measurements of pressure, displacements, and flow rates with both mean values and pulsatile amplitudes in mind. Whats more, all previous MPET studies have fixed the displacement on the cortical surface, which is a crude approximation, as the pulsatile variation in intracranial pressure (ICP) has been shown to depend heavily on the expansion and contraction of brain tissue.

In this thesis, a novel method to model intracranial pulsatility is introduced. The method includes a three-network MPET model of the brain, coupled with a compartment model that represents ICP in the subarachnoid space (SAS) and in the cerebral ventricles. The compartment model is non-linear due to the exponential intracranial pressure-volume relation caused by the rigid confines of the skull. Furthermore, traction boundary conditions are used on the brain surfaces instead of fixed displacements, which allows for the motion of brain tissue along with net CSF exchange to directly drive the pulsatile pressures of the compartment model. The poroelastic domain of the brain is solved using the finite element framework FEniCS, with an implicit Euler scheme in time.

The results of the proposed model are compared and discussed with clinical measurements of pulsatility. The pressure characteristics of the numerical results agree well with clinical data in all three fluid networks and in the compartment model. Displacements and flow rates are also in good agreement with several clinical indicators. This thesis demonstrates the possibility of recreating the observed relation between ICP, deformation, and fluid flow using the proposed model. The thesis also illustrates that modeling pulsatility with MPET models requires a component that accounts for the non-linear relation between brain expansion, CSF flow, and ICP.

Acknowledgements

Contents

Figures

Tables

Chapter 1

Introduction

1.1 Motivation

The dynamic motion of cerebral blood, cerebrospinal fluid (CSF), and brain displacements are characterized by variations in arterial blood pressure induced by the cardiac cycle. This cardiac-induced pulsatile motion, further referred to as pulsatility, is also the main source of fluctuations in intracranial pressure (ICP)[1]. Alterations in CSF flow and ICP are relevant for the diagnosis and treatment of various diseases and injuries to the central nervous system[2]. Some of these include neurodegenerative diseases[3], hydrocephalus[4, 5], and traumatic brain injury [6]. For instance, assessing the ICP amplitude have proven effective in selecting shunt surgeries for patients with possible idiopathic normal pressure hydrocephalus[7]. Furthermore, a better understanding of the pulsatile flow of CSF in and around brain tissue can help develop new treatments using targeted drug delivery[8].

Increasing the understanding of intracranial pulsatility is also relevant when considering the more recent glymphatic theory. For example, CSF enters the brain along periarterial spaces according to this theory. However, the pumping mechanism that drives this influx is uncertain. Although respiratory cycling likely influences flow in perivenous spaces [9] and regulation of ventricular flow rates [10, 11], periarterial CSF flow has been shown to be induced by the cardiac cycle[12, 13]. This pumping mechanism has been hypothesized to not only drive the oscillatory motion of CSF, but also net flow into periarterial spaces [14, 15].

In recent decades, computational modeling has proven to be a useful tool for studying intracranial dynamics[16]. However, several challenges arise when pulsating components are included in these computational models. The rapid change in arterial blood pressure induces large temporal gradients that can lead to numerical instabilities. In addition, models that include pulsatile components require a more extensive validation process, since both pulsatile and time-averaged quantities should comply with clinical measurements. As such, developing new modeling

1

frameworks that are both stable and easily validated is an important step for further studies on intracranial pulsatility.

1.2   Previous Work

Several studies suggest that influx of CSF into the parenchyma occurs along periarterial spaces [12, 17, 18]. Observations of faster movement of tracers in perivascular spaces following increased arterial blood flow indicate that arterial pulsations are the main driver of periarterial flow[19, 20]. In addition, a bulk flow of interstitial fluid (ISF) has been suggested in the extracellular space (ECS) between periarterial and perivenous spaces[21]. However, the routes for waste clearance and outflow are still debated and studies have found varying results. For example, Carare et al. [22] suggest that solutes drain out of the parenchyma following the basement membranes of capillaries and arteries in the opposite direction of blood flow. Iliff et al. [17] demonstrated how a portion of the ISF is drained from the brain parenchyma along perivenous pathways.

Multiple studies employing numerical modeling have also emerged over the years to help further differentiate this understanding. Some studies have focused on direct modeling of flow in perivascular spaces. For example, Vinje et al. [23] demonstrated how a higher rate of transport of tracers along pial periarterial spaces than perivenous spaces can be explained by the difference in their respective geometries. Daversin-Catty et al. [24] and Kedarasetti et al. [25] studied the mechanisms that are likely to govern the flow of fluid in perivascular spaces (PVS), using a moving pulsatile inner boundary for the arterial wall. Kedarasetti et al. [26] also studied whether arteriol vasodilation can drive convective flow through the ECS.

Other computational studies have focused on modeling fluid transport throughout the brain parenchyma and in the surrounding fluid-filled cavities. Causemann et al. [27] used a coupled Biot-Stokes model for poroelastic brain deformation and CSF flow in the ventricles and the subarachnoid space (SAS) using a patient-specific geometry. Vardakis et al. [28, 29], Guo et al. [30–32] and Chou et al. [33] have used multiple-network poroelastic theory (MPET) to model fluid flow in the parenchyma, following the original work of Tully and Ventikos [34]. MPET studies on the brain include various fluid pressures to model several communicating networks such as arteries, veins, capillaries, perivascular spaces, and extracellular spaces. These studies typically relate variations in macroscale geometry, blood waveforms, or other patient-specific properties to changes in pressures and flow rates. MPET models do not account for microscale variations in the geometry of different types of vessels and fluid spaces, and instead treat the whole brain as a continuous domain.

1.3   Missing Work

The use of MPET models has proven promising for studying the interaction between parenchymal fluids and tissue. Some of these studies have modeled changes in pressure over hours [33] or even days[34] and have neglected any pulsatile components. Other studies have included patient-specific pulsating blood flows [28–31] as boundary conditions for the arterial blood network. These studies usually report on the resulting pressures and velocities of fluid networks after a periodic steady-state solution is obtained. However, no attempts have been made to rigorously relate both the pulsatile pressure curve of each network and the time-averaged pressures to clinically measured values.

One challenge that arises when studying MPET models is the application of appropriate boundary conditions[35]. The application of realistic boundary conditions to these types of mixed system is not straightforward, especially when traction-type boundary conditions are considered[36]. All previous studies using MPET to model the brain have used a no-slip condition on the outer surface of the brain. This is a crude approximation as the mean thickness of the subarachnoid space (SAS) is about 3 mm[37], while the maximal measured tissue displacement is in the range of $0.1 - 0.5$ mm[38–40]. Applying a traction-based boundary condition on both the outer brain surface and the ventricular wall could be a better approach, but it has not yet been attempted.

1.4   Scope of Work

Given the lack of studies that relate MPET models with brain pulsatility, the aim of this thesis is to investigate to what extent it is possible to obtain an MPET model that can replicate the pulsatile pressure of multiple fluid networks in the brain. The MPET model of this study will be limited to modeling only three fluid networks at a time to focus attention on accurately replicating the pulsating pressures in these three networks. In addition, two significant alterations will be made from previous MPET studies. The first is that a traction boundary condition will be used on both the inner ventricular surface and the outer surface that borders the SAS. The other modification is the use of a non-linear compartment model for the ICP which will govern the boundary conditions of the MPET model. A non-linear model is used because of the exponential volume-pressure curve invoked by the rigid cranium.

The thesis will also present relevant theory with respect to brain physiology and mathematical methodology. The results of the model will also be presented along with a discussion of the results. The discussion will assess to what extent the resulting model replicates clinical measurements of various quantities and will also compare how the results fit with current studies on the glymphatic system.

Chapter 2

Anatomy of the Brain

This chapter presents general brain anatomy with an emphasis on the biological systems that are relevant to this thesis. As such, special attention is paid to the systems that govern the macroscale mechanical dynamics of the brain. In this context, the macroscale refers to a scale that describes the dynamics of the whole brain organ, as well as the interplay with the fluids that surround and interact with the brain. However, as some processes are inherently multiscale, emphasis will also be placed on certain microscale processes such as fluid velocities inside brain tissue and rates of fluid exchange between compartments.

If not stated otherwise, the following theory of brain anatomy is gathered from the book "Primer on Cerebrovascular Diseases (Second Edition, 2017)"[41] while general cardiovascular physiology is from the book "Medical Physiology (Third Edition, 2016)"[42].

2.1   Brain parenchyma

The brain is located inside the cranial cavity and together with the spinal cord constitutes the central nervous system. The brain parenchyma refers to the functional tissue of the brain. At the cellular level, it is made up largely of two types of cells: glial cells and neurons. Neurons are the cells responsible for sending and receiving nerve impulses, and brain activity is made possible by the interconnections of neurons. Glial cells provide support for neurons and help maintain general homeostasis in the brain. In addition, the brain contains different extracellular fluids that permeate the brain through separated compartments. These fluids are (most notably) blood plasma, ISF, and CSF. Blood networks penetrate the parenchyma through arteries, veins, and capillaries and are separated from brain cells through the blood-brain barrier (BBB). The BBB is a diffusion barrier made up of endothelial cells, endothelial astrocyte end-feet, and pericytes that allows certain molecules such as O_2 and CO_2 to pass through passive diffusion. Essential metabolic products are also transported selectively and actively through

4

the BBB, while unwanted solutes are excluded[43].

ISF surrounds and bathes cells in the brain parenchyma and drains into the CSF that fills the larger spaces of the central nervous system[44]. The subarachnoid space (SAS) is a thin space filled with CSF that lies between the outer surface of the brain parenchyma and the skull. As the SAS completely encapsulated the parenchyma, it acts as a protective cushion for the brain. The ventricles of the brain are CSF-filled cavities located on the inside of the brain in the center of the cranial cavity. A large portion of the CSF is produced inside the ventricles by the choroid plexus[45]. The SAS is connected to the ventricles through a series of canals that lead to the fourth ventricle, which is connected to the rest of the cerebral ventricles through the cerebral aqueduct. The SAS is also connected to the spinal SAS, which is located outside the cranial vault. Similarly to how the SAS surrounds and protects the brain, the spinal SAS is filled with CSF and surrounds the spinal cord. An illustration of the brain parenchyma, together with the CSF-filled spaces inside the cranium, can be seen in Figure 2.1
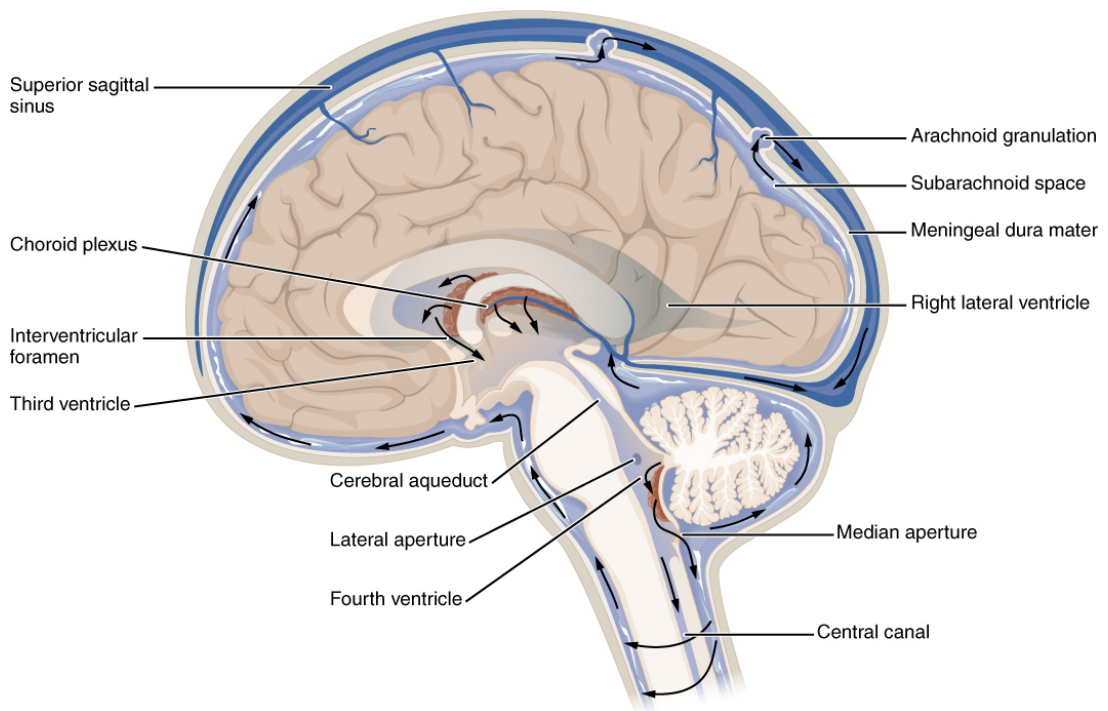
Figure 2.1: Basic anatomy of the brain with an emphasis on components related to the cerebrospinal fluid (CSF) system. Figure adopted from[46, p. 6]
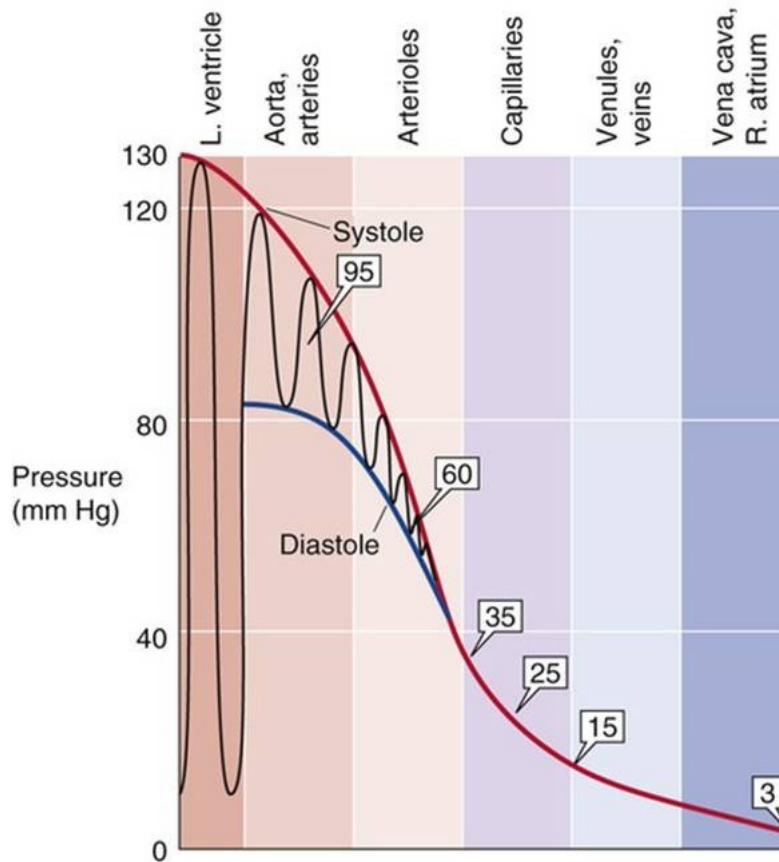
Figure 2.2: Illustration of the pressure profile of blood pressures in the systemic circulation. Figure adopted from[42]

2.2 Intracranial Pulsatility

Fluid flow through the intracranial cavity is characterized by the skull acting as a rigid container. The Monro-Kellie doctrine [47, 48] hypothesizes that the total volume of content within this space must remain constant. The hypothesis follows from the assumption that intracranial fluids and brain tissue within the closed cranial cavity are (nearly) incompressible. Intracranial dynamics is governed by the demand of volume from the intracranial contents, and increasing one volume will lead to a decrease in others. These intracranial contents are (most significantly) arterial blood, arteriole/capillary blood, venous blood, brain tissue, and CSF/ISF, and their interaction governs the spatial and temporal variation of intracranial pressure (ICP). Another unique effect caused by the rigid skull is that any variation in ICP is felt almost instantaneously throughout the cranium. As such, the pressure waveform of the parenchymal tissue and the surrounding CSF tends to be similar and independent of spatial location[2]. This does not apply to cerebral blood networks, which are characterized by the pressure profile of the systemic

circulation, illustrated in Figure 2.2. This profile is a general characterization of systemic blood network pressures in close proximity to the heart and does not directly represent cerebral blood pressures. Throughout this thesis, a horizontal body posture is assumed such that hydrostatic pressure differences can be neglected. The only significant difference from the pressure profile in Figure 2.2 and cerebral blood pressure is the added resistance of blood flowing to the head. As such, the systemic blood pressure profile can be thought of as an upper bound for the equivalent cerebral blood pressures.

The main driver of intracranial pulsatility stems from the cardiac cycle. As the heart ejects blood during systole, the arterial pressure increases throughout the body. The volume of blood inside the cranium increases during systole as the arterial inflow exceeds the venous outflow. Subsequently, the increase in blood volume induces the motion of the CSF and the expansion of the brain parenchyma. An important mechanism that governs intracranial pulsatility is intracranial compliance, which describes the ratio of volume change to pressure change inside the cranium. This compliance consists of four main components, which are arterial compliance, venous compliance, brain tissue compliance, and spinal sac compliance[2]. As the brain parenchyma is almost incompressible and the blood and CSF are completely incompressible, they display limited pressure regulation on their own. The main source of pressure regulation for ICP is the spinal SAS[1] which communicates with the ICP by regulating the volume of CSF inside the cranium and providing a damping mechanism through the compliance of the spinal sac. Mararou et al. [49] where the first to determine an exponential relationship between ICP and variation in craniospinal volume content through experiments. This relationship has since been verified and also quantified for the spinal SAS[50][51]. An illustration of this exponential relationship is shown in figure 2.3
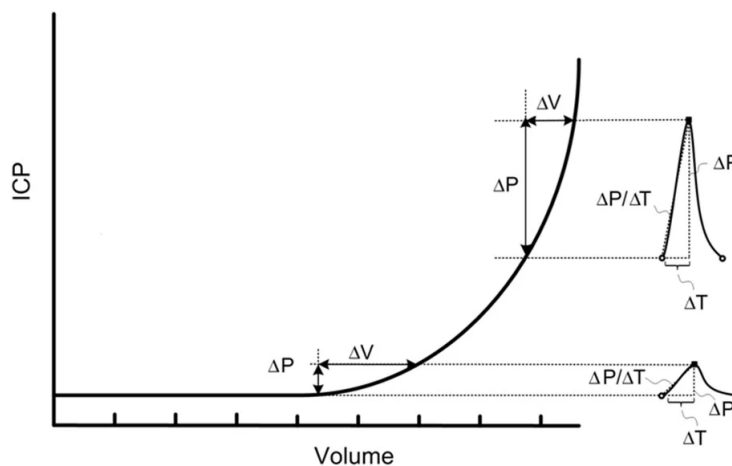
Figure 2.3: Illustration of the exponential relationship between intracranial pressure (ICP) and craniospinal volume. Figure adopted from[2]

Baledént [1] measured intracranial blood flow and CSF circulation using Phase-Contrast Magnetic Resonance Imaging (PC-MRI). These measurements and their correlations were used to hypothesize a relationship between blood volumes, brain expansion, and CSF pulsations during cardiac cycling. As these measurements have been used extensively as references for the development of the model in this thesis, a brief presentation of their hypothesized relationship is presented in the following paragraphs.
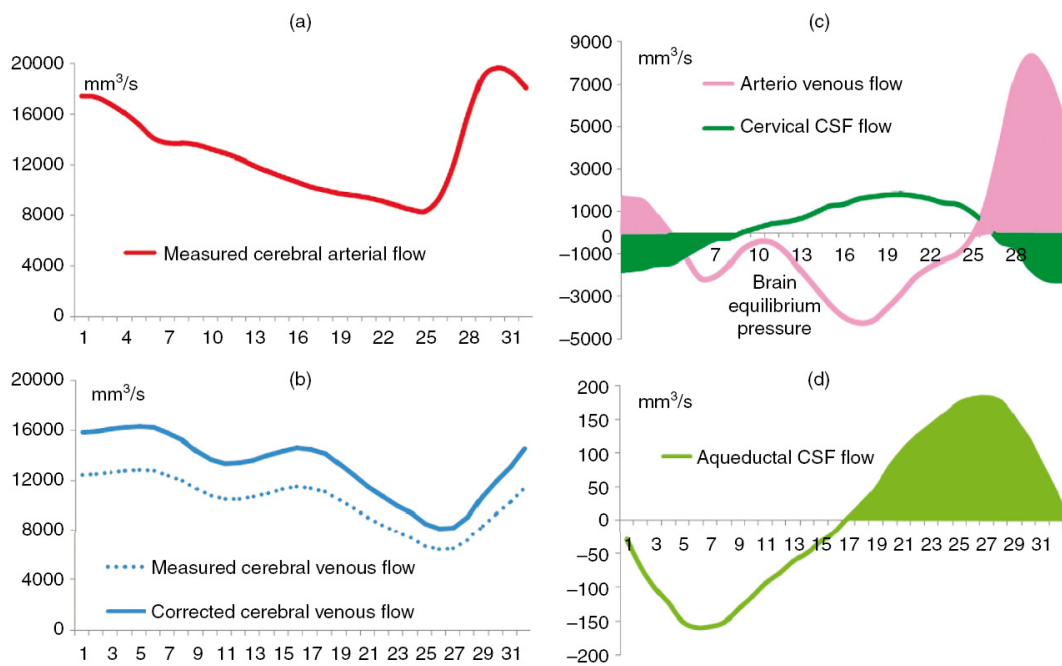
Figure 2.4: Diagrams of flow curves during a cardiac cycle measured in a healthy 30-year-old woman. The various plots show: Total cerebral arterial flow into the cranium (a) Cerebral venous flow out of the cranium (measured and corrected) (b), Cervical CSF flow (flow into the cranium from the spinal CSF compartment) and net blood flow (arterial inflow minus venous outflow) (c), Aqueductal CSF flow, positive direction into the ventricles (d). Figure adopted from[1]

Figure 2.4 shows the results of the PC-MRI measurements in a 30-year-old woman representing a normal healthy individual. The x-axis of all four plots shows the temporal resolution of the images used to generate the measurements (32 over one cardiac cycle). The plot on the upper left shows the cerebral arterial flow curve with the systolic phase starting approximately at the 25th image. The curve shown is the sum of the flow from the four main arteries leading to the cranial vault. In the graph showing the measurement of cerebral venous outflow, a corrected curve was added as the smaller veins were not measured. The corrected curve was calculated based on maintaining net zero blood flow over each cardiac cycle. The plot in the upper right shows two curves: The cervical CSF curve

shows the flow of CSF that enters the cranial vault from the spinal CSF compartment. The arterio venous curve is the net flow of blood into the cranium (arterial inflow minus corrected venous outflow) and illustrates that the total volume of intracranial blood is not constant. The net inflow of blood pulsates in opposite phase with the outflow of CSF, and the plot demonstrates how the flow volumes balance each other to maintain a constant total intracranial volume, as postulated by the Kellie-Monroe doctrine. The plot on the lower left shows the aqueductal CSF curve, which is the amount of CSF that flows from the fourth ventricle to the third ventricle. The aqueductal stroke volume can be seen colored in solid green and is the total flow that enters this channel during a cardiac cycle. This volume was found to be strongly correlated with the timing of peak venous outflow, indicating a direct relationship between brain expansion and ventricular pulsation.

Figure 2.5 shows a series of drawings that illustrate how the measured flows interact with each other, during the systolic phase of the cardiac cycle. Baledént [1] gave the following explanation for the series of events pictured in the illustration; The sudden increase of cerebral blood volume during early systole (image 1) will rapidly expand the parenchymal volume towards the skull. The low viscous CSF will then be flushed downward and into the spinal SAS (image 2), which acts as a pressure dampener, as explained earlier. The increased blood volume then induces a peak in venous outflow, and CSF is subsequently flushed from the fourth ventricle into the SAS (image 3) and from the third ventricle to the fourth ventricle through the aqueduct (image 4). A transient equilibrium occurs (image 5) before spinal CSF flows upward to fill the SAS and the cerebral ventricles during the diastolic phase following a decrease in blood volume and ICP.
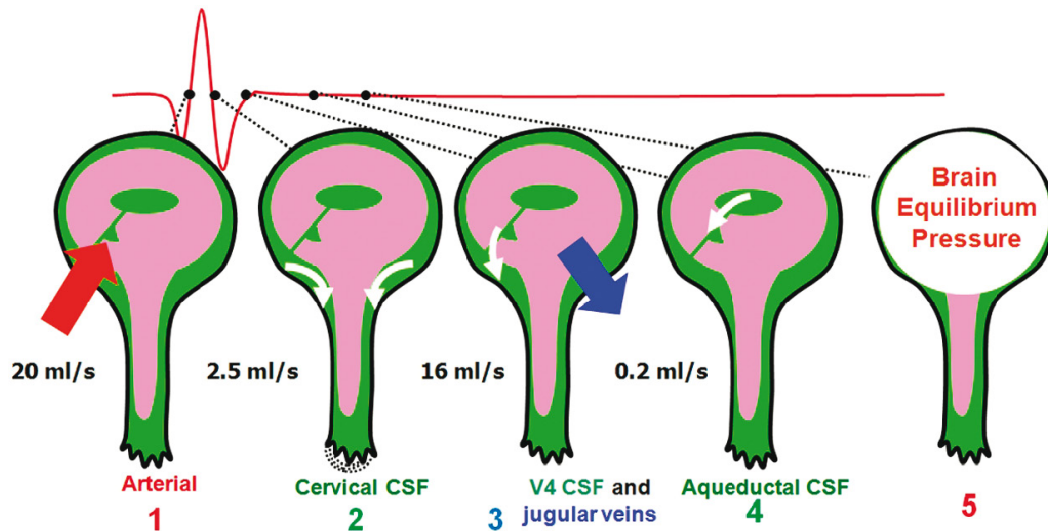
Figure 2.5: A series of drawings that illustrate intracranial dynamics during the systolic phase. Figure adopted from[1]

2.3   Waste clearance and the Glymphatic Theory

The flow of ISF and CSF plays several important roles in brain homeostasis, such as providing its cells with suitable ions and nutrients. Another important mechanism of the CSF and ISF is the waste clearance system of the brain. The lymphatic system handles the removal of metabolic waste in all parts of our body, except in the brain. The brain lacks lymphatic channels and waste clearance is still a subject of debate. The more recent glymphatic theory suggests that CSF is circulated through the brain following perivascular spaces, where it interacts with ISF in the extracellular space in the brain. Perivascular spaces are fluid-filled channels that circumferentially surround certain blood vessels and serve multiple functions[17, 52]. The general theory hypothesizes that CSF is transported into the brain parenchyma through periarterial spaces surrounding the arteries that penetrate the parenchyma. The CSF then combines with ISF before it is drained out through perivenous spaces. Note that the exact pathways and mechanism of metabolic clearance are disputed, and several different mechanisms are likely to contribute to this system. Inside the extracellular tissue of the brain, the interstitial solutes are transported by a mix of diffusion and bulk flow. An illustration of the suggested pathway for waste clearance following the glymphatic theory can be seen in Figure 2.6.
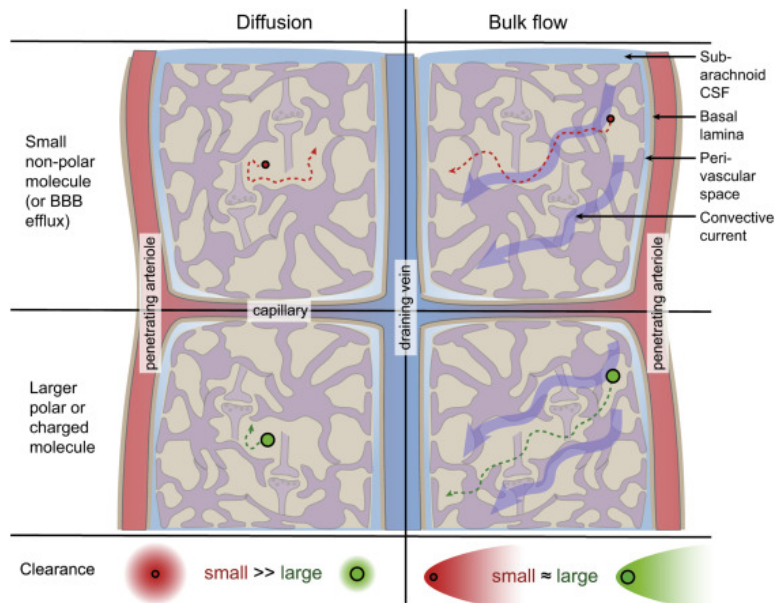
Figure 2.6: Illustration of the flow of CSF following the glymphatic theory. Figure adopted from [53]

The figure illustrates how the solutes in the extracellular tissue are transported by a mix of diffusion and bulk flow. It also shows how smaller nonpolar molecules diffuse more rapidly than larger molecules, while for bulk flow the solutes are cleared at the same rate independent of molecular size[53]. This waste clearance system

is hypothesized to be important for several neurodegenerative diseases such as Alzheimer's and Parkinson's. These diseases can be identified by an increase of protein aggregations in the brain tissue[54]. Although the exact reason for the accumulation of these aggregations is still not known, it is hypothesized that a decrease in the metabolic waste clearance function of the brain can contribute to these diseases[55].

Chapter 3

Mathematical Modeling of Brain Pulsatility

In this chapter, the mathematical model used in this thesis is presented. The mathematical theories for the model are derived, and explanations for how the model aims to replicate brain pulsatility are given. This thesis combines two type of models into one coupled model. The coupled model aims to recreate pulsatility in the cranium as a whole. As explained in the previous chapter, intracranial pulsatility depends not only on the pulsating dynamics of the brain parenchyma, but also its interaction with the CSF that fills the cavities surrounding the brain. The pulsating behavior of the parenchyma is represented by a set of governing equations derived from Biot's theory of poroelasticity[56]. These equations are applied onto a geometrical realistic representation of the brain and are solved using FEM. The second part of the combined model represents the CSF-filled cavities surrounding the brain. These cavities use lumped modeling to represent the pulsating fluid pressures in the various CSF compartments. The fluid pressures in the lumped model are driven by the pulsations from the brain parenchyma and essentially act as boundary conditions for the poroelastic model. As such, details on how these two models interact and depend on each other will be given. Later in this thesis, the numerical algorithms used to solve the coupled model will be presented.

3.1 Poroelastic Theory

As mentioned, Biot's theory is used to model the brain parenchyma. The mathematical derivation of these equations follows.

3.1.1 Biot's Consolidation Theory

Biot's three-dimensional consolidation theory describes the settlement of soil under load by a consolidation process[56]. The general theory assumes isotropic

material, linear and reversible strain-stress relationship, small strains, and incompressible fluid contained in the soil material. In addition, the fluid is assumed to flow through the porous skeleton according to Darcy's law. Consider an instantaneous flux of fluid V_i in a porous medium with a pressure p that describes the fluid pressure. Darcy's law governs the porous flow of the liquid

$$\boldsymbol{V} = -K\nabla p \tag{3.1}$$

where $K = \frac{\kappa}{\mu_f}$ is the hydraulic conductivity tensor, where κ and μ_f represent the permeability of the porous skeleton and the viscosity of the fluid, respectively. It is emphasized that throughout this thesis, bold symbols will be used to denote vectors and tensors. The incompressible fluid entering the surface of a unit of soil must balance the fluid contained within the unit soil; hence the continuity equation of liquid transport is described as

$$\dot{\theta} + \operatorname{div}\boldsymbol{V} = 0 \tag{3.2}$$

in which θ describes the increment in liquid volume per unit volume of soil and is referred to as the variation in liquid content. Using Hooke's law combined with the potential energy of a unit of soil, θ can be expressed as

$$\theta = \alpha\operatorname{div}\boldsymbol{u} + Sp \tag{3.3}$$

The first term on the right-hand side represents the increase in soil volume, in which α refers to the Biot-Willis coefficient, which measures the ratio of water volume that escapes from the total volume if the latter is compressed. Note that in this equation $\boldsymbol{u}$ is a vector that describes the solid displacements of the porous skeleton. Hence, the divergence of this vector corresponds to the relative variation of soil volume. The second term represents the amount of liquid that can be forced into a unit of soil under a pressure p, when the volume of the soil remains constant. S is the specific storage coefficient and specifies the amount of fluid that can be stored in a unit of soil. These derivations (and proofs) are quite long and arduous, and the reader is referred to [56] for further details. Combining Equation (3.1) and Equation (3.3) with the continuity equation for liquid (3.2) yields the following equation for mass conservation

$$\operatorname{div}(K\nabla p) = \alpha\operatorname{div}\dot{\boldsymbol{u}} + S\dot{p} \tag{3.4}$$

To derive the equation that describes the conservation of momentum for Biot's consolidation theory, it is first convenient to describe the total stress tensor as a function of the stresses caused by elastic deformation and the internal liquid pressure

$$\boldsymbol{\sigma} = 2\mu\boldsymbol{\epsilon} + (\lambda\operatorname{div}\boldsymbol{u} - \alpha p)\boldsymbol{I} \tag{3.5}$$

where $\boldsymbol{\sigma}$ is the total Cauchy stress tensor, and $\boldsymbol{\epsilon}$ is the small-strain tensor defined as

$$\epsilon(\boldsymbol{u}) = \frac{1}{2}(\nabla \boldsymbol{u} + (\nabla \boldsymbol{u})^\top) \tag{3.6}$$

The relation between elastic deformation and corresponding stresses follows from Hooke's law, in which λ and μ are the standard Lamè parameters for an isotropic and homogeneous material. Balancing the total stress acting on a small volume of soil with the external forces acting on the soil body yields the following formulation

$$-\operatorname{div} \boldsymbol{\sigma} = \boldsymbol{f} \tag{3.7}$$

which together with Equations (3.4) to (3.6) constitute the governing equations for the classical Biot's consolidation problem with the unknowns: $\boldsymbol{u}$ and p. In general, this model is used to describe the behavior of a single porosity and single permeability medium such as a non-fractured reservoir with uniform porosity and permeability[57].

3.1.2 Multiple-network Poroelasticity with a Total Pressure Formulation

Biot's consolidation theory can be extended to include several separate fluid networks, each with its own fluid pressure. For example, fractured rock can be considered as such a medium, with fractures and intervening porous blocks describing two separate fluid networks of the system [58]. Given a system with an arbitrary number of fluid networks M, the force balance of such a system can be formulated as

$$-\operatorname{div}\left(2\mu\boldsymbol{\epsilon} + (\lambda \operatorname{div} \boldsymbol{u} - \sum_{m=1}^{M} \alpha_m p_m)\boldsymbol{I}\right) = \boldsymbol{f} \tag{3.8}$$

where p_m and α_m represent the fluid pressure and the Biot-Willies coefficient of fluid network m, respectively. The equation for mass continuity (3.4) is now extended to M individual equations, so that mass is conserved in each separate network. By rearranging and adding a source term and a transfer term, the equations take the form:

$$S_m \dot{p}_m + \alpha_m \operatorname{div} \dot{\boldsymbol{u}} - \operatorname{div}(K_m \nabla p_m) + \gamma_m = g_m \tag{3.9}$$

where g_m is a source term and γ_m is a transfer term that quantifies the transfer of liquid out of network m and into other fluid networks. Fluid transfer between networks will depend on the pressure difference between the networks. If this transfer is assumed to be linearly proportional to the pressure difference, the transfer term takes the following form

$$\gamma_m = \sum_{i=1}^{M} \eta_{m \leftarrow i}(p_m - p_i)$$

in which $\eta_{m \leftarrow i}$ is the transfer coefficient of the fluid that is transferred from network m to network i. Equation (3.8) and Equation (3.9) originate from the multiple network poroelastic theory (MPET) and describe the deformation and flow of liquid in a linearly elastic porous solid with multiple fluid networks permeating the solid matrix. In more recent work, this formulation has been modified to alleviate instability for solid materials that are nearly incompressible [59] [60]. This formulation introduces an additional total pressure variable p_0, in addition to the fluid pressures for each segregated fluid network. The total pressure is defined as

$$p_0 = \lambda \text{div } \boldsymbol{u} - \sum_{m=1}^{M} \alpha_m p_m \qquad (3.10)$$

By further introducing $\alpha_0 = 1$ to allow for the short-hand notation of the sum of pressures as $\alpha \cdot p = \sum_{m=0}^{M} \alpha_m p_m$, and combining Equations (3.8) to (3.10), a general system of MPET equations is defined as

$$-\text{div} \left(2\mu\boldsymbol{\epsilon} \right) - \nabla p_0 = \boldsymbol{f}, \qquad (3.11a)$$

$$\text{div } \boldsymbol{u} - \lambda^{-1}\alpha \cdot p = 0 \qquad (3.11b)$$

$$S_m \dot{p}_m + \alpha_m \lambda^{-1}\alpha \cdot \dot{p} - \text{div}(K_m \nabla p_m) + \gamma_m = g_m \quad m = 1, 2, ..., M \qquad (3.11c)$$

3.1.3 Boundary Conditions for the Poroelastic Problem

The equations in (3.11) require a set of boundary conditions to close the problem. These are usually represented in the form of Dirichlet boundary conditions, Neumann boundary conditions or Robin boundary condition, which is a mixture of the two former conditions[61]. A brief explanation of the different types of boundary condition used in the thesis and their physical interpretation follows.

For the momentum equation in (3.11a), a common option is to set the displacements directly on the boundary using a Dirichlet condition. Another common option is to prescribe traction onto the boundary through a Neumann condition. In this system, the Neumann condition is a natural boundary condition in the momentum equation, since the prescribing term occurs naturally in the weak formulation of the problem[62]. As an example, the poroelastic domain is imagined to be encapsulated in some stationary fluid with the fluid pressure p_f acting on the domain boundary. A traction boundary condition for the momentum can then be defined as

$$\boldsymbol{\sigma} \cdot \boldsymbol{n} = p_f \boldsymbol{n} \quad \text{on} \quad \partial\Omega$$

with $\boldsymbol{n}$ being the normal unit vector on the boundary surface, and the stress tensor now defined as: $\boldsymbol{\sigma} = 2\mu\epsilon(\boldsymbol{u}) + p_0 \boldsymbol{I}$.

The boundary conditions applied to the fluid networks in Equation (3.11c) determine the amount and direction of fluid flowing over the boundary, according to Darcy's law. If the fluid pressure is applied directly with a Dirichlet condition, the fluid flow is determined indirectly by the resulting pressure gradient at the boundary. If a natural Neumann condition is used instead, the pressure gradient is specified directly, which is equivalent to directly specifying the flow of fluid on the boundary. The poroelastic domain is again imagined to be encapsulated in some fluid. A natural assumption for fluid exchange over the boundary is to assume that the flow is proportional to the difference in pressure between the surrounding fluid p_f and the pressure on the boundary of the respective fluid network. Such an assumption can be implemented by using a Robin boundary condition defined as

$$-K_m \nabla p_m \cdot \boldsymbol{n} = \beta_m (p_m - p_f) \quad \text{on} \quad \partial \Omega \quad m = 1, 2, ..., M$$

in which $\beta_m \geq 0$ describes the boundary permeability of fluid network m. As mentioned above, the Robin condition constitutes a mixture of Dirichlet- and Neumann-type boundary conditions. This can be exemplified by assessing the extreme values of the boundary permeability. In the case when β_m is equal to zero, the boundary is completely impermeable, and the boundary condition for the fluid pressure reduces to a Neumann condition with zero flux. In the other extreme case, when the boundary permeability approaches infinity, a Dirichlet boundary condition emerges. This follows as the Neumann boundary condition on the left-hand side becomes comparably small and vanishes such that the fluid network pressure equals the boundary pressure.

Singular System   Applied forces can induce domain movement, and prescribing some displacements will ensure that the object is anchored in place and only allowed to deform relative to itself. However, applying such displacements relies on partial knowledge of the problem solution, which may not always be available. In the case where pure Neumann boundary conditions are applied and no displacements are prescribed in the domain, the problem can become singular unless both the net force and the net torque acting on the body are zero[63]. If the net force and torque are non-zero, the problem will have infinite possible solutions, owing to the rigid body motion (RMB) of the domain. For many types of analysis, RBM is undesirable and techniques to remove RBM must be applied to obtain a non-singular system. One such technique uses Lagrange multipliers that ensure that the displacements of the system are orthogonal to the function space of the RBM. This technique was applied to the model in this thesis, which was necessary since the pure Neumann boundary conditions were used for the momentum equation. The reader is referred to the articles by Bochev[64] et al. and Kuchta[63] et al. for further theoretical details on how this method is implemented for linear elasticity problems.

3.2   Mathematical Model

To formulate a model that fully represents the dynamics of intracranial pulsatility, the problem is divided into two separate components. The first component is the brain parenchyma, modeled as a poroelastic domain described by a set of MPET equations. The second component is the CSF-filled cavities that encapsulate and exchange CSF with the brain parenchyma, represented by a lumped model. The physical nature of the two components will be explained and a coupling between the two components will be proposed.

3.2.1   Poroelastic Modeling of the Brain
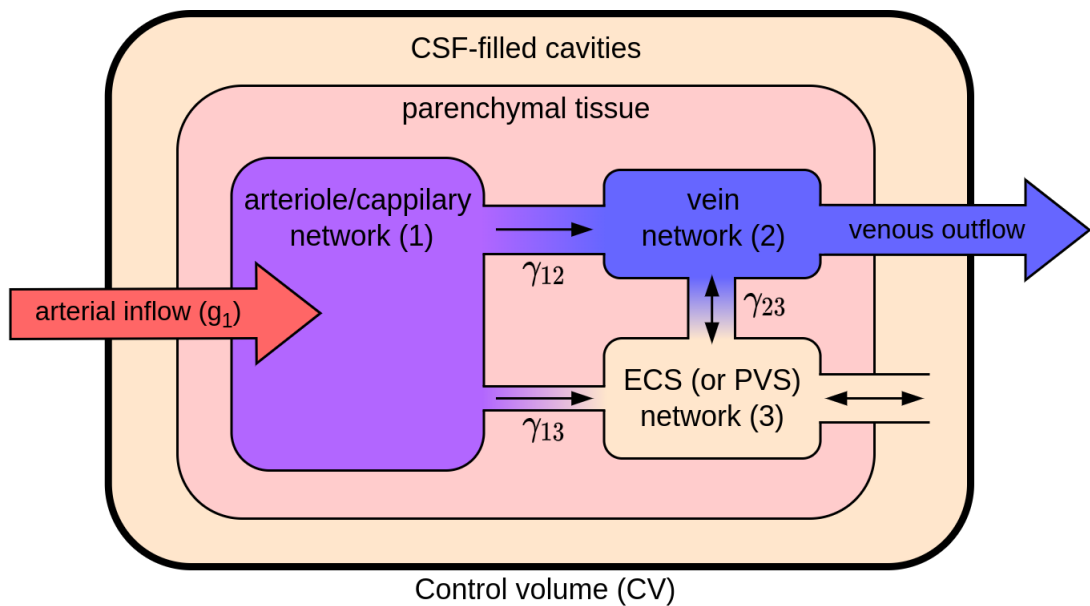
Figure 3.1: Schematic illustration of fluid paths in the MPET brain model. The arrows in the illustration indicate the directionality of the fluid flow.

The MPET system of equations in (3.11) is used to model the interaction of fluid flow and displacements of parenchymal tissue in the brain. The model includes three different fluid networks ($M = 3$); one network that represents blood flow in a range of smaller arterioles to larger capillary blood vessels ($m = 1$), one network that represents blood flow in the smaller veins ($m = 2$), and one network that models the flow of CSF/ISF in the PVS or the ECS, depending on the test case ($m = 3$). The arteries are not included as a separate fluid network in this model. Instead, the pressure and flow generated by arterial pulsations are represented as a source term (g_1) that is applied directly to the arteriole network. Arteriole and capillary blood vessels are assumed to be evenly distributed throughout the brain parenchyma compared to the larger arteries, which are located primarily on the outer surface of the brain [41]. Therefore, the pulsating source term is

applied uniformly throughout the brain. This source term is the only driver of pulsatility in the model, and all deformation and pressure variation will be driven by this term. From the arteriole network, blood can flow directly into the vein network, or some portion of the fluid contained in the blood can be transferred to extracellular/perivascular spaces. In addition, fluid is transferred between the vein network and PVS/ECS network, which is necessary to maintain the mass balance of the system. The transfer of liquid between the various compartments is quantified by the transfer terms γ_1, γ_2 and γ_3, which are calculated as

$$\gamma_1 = \gamma_{12} + \gamma_{13} \tag{3.12a}$$

$$\gamma_2 = \gamma_{21} + \gamma_{23} \tag{3.12b}$$

$$\gamma_3 = \gamma_{31} + \gamma_{32} \tag{3.12c}$$

$$\gamma_{ij} = \eta_{i \leftarrow j}(p_i - p_j) \tag{3.12d}$$

The fluid accumulated in the arteriole network is transported out of the brain domain through the vein and the ECS/PVS network. An illustration of fluid transport in the model is shown in Figure 3.1

The figure illustrates how excess fluid in the vein network leaves the control volume of the domain, while excess fluid in the ECS/PVS network is dynamically exchanged with CSF in the cavities surrounding the brain. With the source term and the transfer terms defined and assuming that there are no body forces ($\boldsymbol{f} = 0$), the governing equations for the 3-network MPET system are:

$$-\mathrm{div}\,(2\mu\boldsymbol{\epsilon}) - \nabla p_0 = 0, \tag{3.13a}$$

$$\mathrm{div}\,\boldsymbol{u} - \lambda^{-1}\alpha \cdot p = 0 \tag{3.13b}$$

$$S_1 \dot{p}_1 + \alpha_1 \lambda^{-1} \alpha \cdot \dot{p} - \mathrm{div}(K_1 \nabla p_1) = g_1 - \gamma_1 \tag{3.13c}$$

$$S_2 \dot{p}_2 + \alpha_2 \lambda^{-1} \alpha \cdot \dot{p} - \mathrm{div}(K_2 \nabla p_2) = -\gamma_2 \tag{3.13d}$$

$$S_3 \dot{p}_3 + \alpha_3 \lambda^{-1} \alpha \cdot \dot{p} - \mathrm{div}(K_3 \nabla p_3) = -\gamma_3 \tag{3.13e}$$

Boundary conditions for the MPET domain   To define a set of boundary conditions for the system in (3.13) the brain domain is further defined to have two separate boundaries; one outer boundary adjacent to the SAS and one inner boundary bordering the ventricles. An illustration of the model and its various domains and boundaries is shown in Figure 3.2. Ω represents the poroelastic domain with its boundary decomposed into two parts: $\partial\Omega = \Gamma_{\mathrm{SAS}} \cup \Gamma_{\mathrm{VEN}}$.

The CSF that resides in the SAS and ventricles is assumed to be relatively stationary such that the stresses exerted on the brain surfaces are caused only by the hydrostatic pressure of the fluid. In other words, any viscous forces exerted on the brain from fluid movement are neglected. The fluid that resides in the SAS and the ventricles is represented by two separate fluid pressures, $P_{\mathrm{SAS}}(t)$ and $P_{\mathrm{VEN}}(t)$. These pressures are assumed to have no spatial variance within their
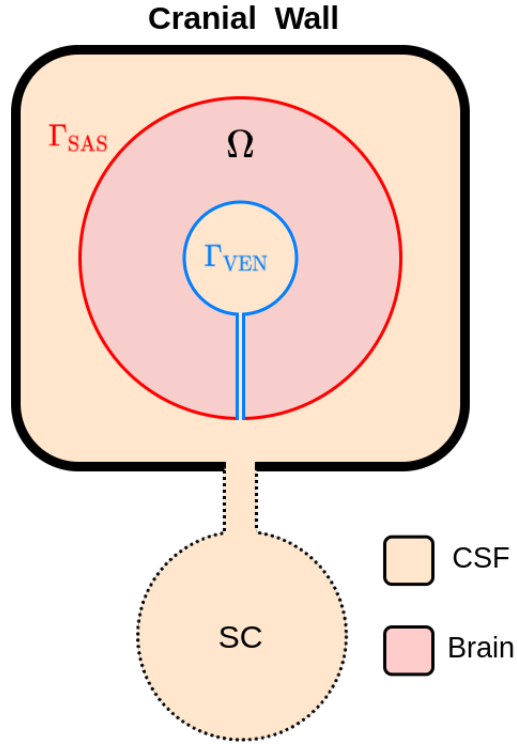
Figure 3.2: Illustration of the computational domain of the model. Ω denotes the poroelastic domain governed by the MPET equations. Γ_{SAS} and Γ_{VEN} are defined as the boundary surfaces of the SAS and ventricles, respectively. SC denotes the spinal compartment/spinal-SAS.

own compartments but can vary relative to each other. The following pure Neumann boundary condition is prescribed for the momentum in Equation (3.13a), with each of the two fluid pressures exhibiting normal stress on their respective surfaces

$$\boldsymbol{\sigma} \cdot \boldsymbol{n} = P_{\text{SAS}} \boldsymbol{n}, \quad \text{on} \quad \Gamma_{\text{SAS}}, \quad \boldsymbol{\sigma} \cdot \boldsymbol{n} = P_{\text{VEN}} \boldsymbol{n}, \quad \text{on} \quad \Gamma_{\text{VEN}}$$

As discussed, defining such a boundary condition for the momentum equation will lead to a singular system. Although it could be possible to fix the brain parenchyma in some locations to avoid singularities, choosing the optimal location is not trivial. Previous clinical studies using MRI suggest that some rigid motion of the brain occurs [65] and that small tissue displacements are present throughout the brain [40].

For the arteriole fluid network in Equation (3.13c), it is assumed that all fluid is transferred to the other fluid networks. Subsequently, no fluid is allowed to leave the brain domain over the arteriole network boundary, and therefore a zero-flux Neumann condition is specified on both boundaries as

$$-K_1 \nabla p_1 \cdot \boldsymbol{n} = 0 \quad \text{on} \quad \Gamma_{\text{SAS}}, \quad -K_1 \nabla p_1 \cdot \boldsymbol{n} = 0 \quad \text{on} \quad \Gamma_{\text{VEN}}$$

For the vein network, it is assumed that the fluid only leaves the domain on the outer SAS surface, where most of the larger cerebral veins are located. With a closed ventricular surface, the boundary conditions for the vein network are specified as

$$p_2 = P_{\text{VEIN}} \quad \text{on} \quad \Gamma_{\text{SAS}}, \quad -K_2 \nabla p_2 \cdot \boldsymbol{n} = 0 \quad \text{on} \quad \Gamma_{\text{VEN}}$$

with P_{VEIN} being a constant back pressure of the veins. This lower back pressure is included to induce an outflow of the system in order to maintain mass conservation of the system. For the last network, the boundary conditions are specified on the basis of the test case. For a PVS network, it is assumed that the CSF surrounding the brain is in direct contact with the CSF in the network. The following Dirichlet boundary conditions are then specified as

$$p_3 = P_{\text{SAS}} \quad \text{on} \quad \Gamma_{\text{SAS}}, \quad p_3 = P_{\text{VEN}} \quad \text{on} \quad \Gamma_{\text{VEN}}$$

If an ECS network is specified, it is assumed that fluid exchange between the network and the surrounding CSF faces substantial flow resistance. In this case, the Robin boundary condition is utilized as

$$-K_3 \nabla p_3 \cdot \boldsymbol{n} = \beta(p_3 - P_{\text{SAS}}) \quad \text{on} \quad \Gamma_{\text{SAS}}, \quad -K_3 \nabla p_3 \cdot \boldsymbol{n} = \beta(p_3 - P_{\text{VEN}}) \quad \text{on} \quad \Gamma_{\text{VEN}}$$

with β describing the boundary permeability of the ECS network.

3.2.2 Compartment Model of CSF Pressure

The boundary conditions of the MPET brain model are specified by the pressure of the CSF surrounding the brain. Changes in CSF pressure are instantaneous, almost[11] spatially invariant, and close to the ICP curve. As such, it is further assumed that the CSF pressure in the SAS is equivalent to the ICP. To model the ICP, the exponential pressure-volume relation presented in Marmarou et al. [49] is used. This relation is formulated as

$$\text{ICP}(t) = P_0 \cdot 10^{\Delta V(t)/\text{PVI}} \tag{3.14}$$

in which P_0 defines some baseline ICP, ΔV describes the change in intracranial volume, and PVI is the intracranial pressure-volume index. In contrast to compliance or elastance, PVI describes the relationship between craniospinal volume and pressure throughout the entire physiological ICP range. The exponential relationship in Equation (3.14) will ensure that, for large changes in intracranial volume, the relative change in ICP will be small. In this model, the change in intracranial volume is defined as

$$\Delta V(t) = \int_0^t \left[Q_{\text{SAS}}(t) + \dot{V}_{\text{SAS}}(t) - Q_{\text{AQ}}(t) \right] dt \tag{3.15}$$

with $Q_{\text{SAS}}(t)$ being the rate of CSF exchanged directly between the brain parenchyma and the SAS, and $Q_{\text{AQ}}(t)$ the rate of CSF that flows through the cerebral aqueduct, with a positive direction pointing into the ventricles. $\dot{V}_{\text{SAS}}$ represents the time derivative of the relative deformation of the SAS surface. As mentioned above, the ICP represents the pressure of the CSF in the SAS, which is in direct contact with the surface of the parenchyma. As this surface expands, CSF is displaced into the spinal compartment and the ICP is increased simultaneously. However, the ventricle surface is not in direct contact with this pressure, but is indirectly connected through the cerebral aqueduct, which is represented by the term Q_{AQ} in Equation (3.15). To model this term, the ventricular intracranial pressure (ICPV) is introduced as

$$\text{ICPV} = \text{ICP} + P_{\text{R}} \tag{3.16}$$

in which P_R is the ventricular pressure relative to the ICP. For the expression in Equation (3.16), as well as for the volume expression in Equation (3.15), the following assumptions are made: (1) ICP variations are felt instantaneously throughout the cranium[2], and therefore the ICPV should have a waveform and magnitude similar to the ICP, (2) the spatial gradients of the ICP are small[2, 11] and therefore the magnitude of P_R is small compared to the ICP, (3) the contribution of the cerebral ventricles to the overall regulation of ICP is low compared to the cervical flow of CSF, and (4) the pulsatile motion of CSF through the cerebral aqueduct is driven by surface expansion and the exchange of CSF over the ventricular surface. Assumptions (1), (2) and (3) argue that the expression of ICPV in Equation (3.16) is valid. The last assumption (4) is used to relate the relative pressure P_R directly to the pulsatile motion of the ventricle surface. This relative pressure is modeled through a 2-element linear Windkessel model as

$$C \frac{dP_R}{dt} = \dot{V}_{VEN} + Q_{VEN} + Q_{AQ} \tag{3.17}$$

with C being the additional compliance in the ventricles. R_{AQ} is the resistance of the cerebral aqueduct, $\dot{V}_{\text{VEN}}$ is the time derivative of the deformation of the ventricular surface, and $Q_{\text{VEN}}(t)$ is the rate of CSF exchanged over the ventricular surface. Lastly, the aqueductal flow rate is calculated as

$$Q_{AQ} = \frac{\text{ICP} - \text{ICPV}}{R_{AQ}} = -\frac{P_R}{R_{AQ}} \tag{3.18}$$

with its pulsating flow acting as a direct coupling between the pressure in the SAS and the ventricles.

To summarize the compartment model, the ICP defined in Equation (3.14) and the relative ventricular pressure P_R defined in Equation (3.17) are included to facilitate two main effects. The ICP is included to capture the larger temporal variance induced by cardiac cycles, while the relative ventricular pressure is included to account for any spatial variance in the pressure inside the cranium. An illustration of the compartment model defined by Equations (3.14) to (3.17) can be seen in Figure 3.3
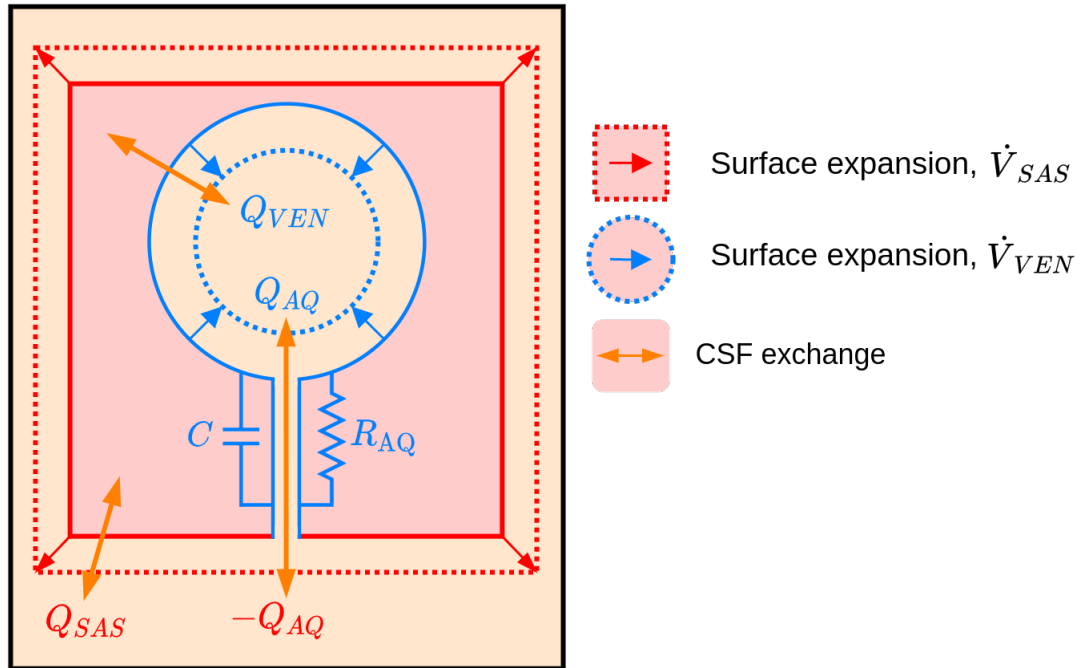
Figure 3.3: Illustration of the compartment model. Red shows the contribution to the ICP modeled by Equation (3.14), while blue demonstrates the contribution to the relative ventricle pressure, modeled by Equation (3.17)

3.2.3 Coupled Model of Intracranial Pulsatility

A brief summary of the combined model follows, and the coupling terms between the MPET model and the compartment model are presented. In addition, the different model configurations used in this thesis are summarized.

The poroelastic model of the brain described by the system of equations in (3.13) is coupled with the compartment model through its boundary conditions summarized in Table 3.1.
The back pressure of the vein network P_{VEIN} is constant, while the pressures in the SAS and ventricles are governed by the compartment model. These pressures are further defined as

Table 3.1: Summary of the boundary conditions for the poroelastic domain Ω.

Equation	Γ_{SAS}, SAS surface	Γ_{VEN}, ventricle surface
Momentum	$\boldsymbol{\sigma} \cdot \boldsymbol{n} = P_{\text{SAS}}\boldsymbol{n}$	$\boldsymbol{\sigma} \cdot \boldsymbol{n} = P_{\text{VEN}}\boldsymbol{n}$
Network 1	$-K_1\nabla p_1 \cdot \boldsymbol{n} = 0$	$-K_1\nabla p_1 \cdot \boldsymbol{n} = 0$
Network 2	$p_2 = P_{\text{VEIN}}$	$-K_2\nabla p_2 \cdot \boldsymbol{n} = 0$
Network 3 (PVS)	$p_3 = P_{\text{SAS}}$	$p_3 = P_{\text{VEN}}$
Network 3 (ECS)	$-K_3\nabla p_3 \cdot \boldsymbol{n} = \beta(p_3 - P_{\text{SAS}})$	$-K_3\nabla p_3 \cdot \boldsymbol{n} = \beta(p_3 - P_{\text{VEN}})$

$$P_{\text{SAS}} := \text{ICP}$$

$$P_{\text{VEN}} := \text{ICPV}$$

with the ICP and the ICPV defined in Equation (3.14) and Equation (3.16) respectively. Several of the terms governing these pressures are again dependent on physical quantities calculated from the poroelastic model. The time derivatives of the expansion and contraction of the brain surface are defined as

$$\dot{V}_{\text{SAS}} = \frac{d}{dt}\int_{\Gamma_{\text{SAS}}} \boldsymbol{u} \cdot \boldsymbol{n} \, ds \tag{3.19}$$

$$\dot{V}_{\text{VEN}} = \frac{d}{dt}\int_{\Gamma_{\text{VEN}}} \boldsymbol{u} \cdot \boldsymbol{n} \, ds \tag{3.20}$$

with the boundaries Γ_{SAS} and Γ_{VEN} for integrals defined in Figure 3.2. Furthermore, the exchange rates of CSF between the brain and CSF-filled cavities are defined as

$$Q_{\text{SAS}} = \int_{\Gamma_{\text{VEN}}} -K_3\nabla p_3 \cdot \boldsymbol{n} \, ds \tag{3.21}$$

$$Q_{\text{VEN}} = \int_{\Gamma_{\text{VEN}}} -K_3\nabla p_3 \cdot \boldsymbol{n} \, ds \tag{3.22}$$

The integrals in Equations (3.19) to (3.22), along with the boundary conditions in Table 3.1 demonstrate how the poroelastic model and the compartment model are combined into one coupled model for intracranial pulsatility.

Model variations In this thesis, three different model variations are used and compared. Variations in the configurations of the PVS and ECS models have already been described in terms of boundary conditions, and it is also noted that the two configurations will have significantly different values for hydraulic conductivity K_3. The PVS configuration is also noted to be the standard configuration

Table 3.2: Summary of the model variations used in this thesis.

Configuration	Description
Standard (PVS) configuration	PVS network and boundary conditions Coupled with the compartment model
ECS configuration	ECS network and boundary conditions Coupled with the compartment model
Standalone (PVS) configuration	PVS network and boundary conditions Uses a constant ICP $= P_0$

on which the main discussion of results will be based. The third configuration was included to test the dependence of the compartment model and to see whether coupling this model to the MPET model is necessary to describe intracranial pulsatility. As such, the third configuration use a constant ICP on the boundaries of the MPET model and excludes the compartment model altogether. The constant ICP is set equal to the value of the baseline pressure P_0. This configuration will be noted as the standalone configuration as it depends only on the MPET system of equations. A summary of these different configurations is listed in Table 3.2

Chapter 4

Physiological Quantities and Material Parameters

This chapter presents the various physical quantities and material parameters that were used to obtain a model that exhibited clinically realistic behavior. As some of the material parameters are highly uncertain or completely unknown, this chapter also explains how these parameters were determined. Some of these uncertain parameters were chosen on the basis of previous work, while others had to be determined through estimates and testing. In addition, the effects of the various parameters on the overall combined model are discussed.

4.1 Clinical Indicators of Intracranial Pulsatility

With a mathematical model describing intracranial dynamics defined in the previous chapter, a set of physiological indicators was needed. These indicators were primarily based on clinical measurements, but in some cases assumptions had to be made. The indicators served two main purposes; they acted as reference values that the mathematical model aimed to replicate, and they were used to estimate several of the model parameters. An overview of these indicators can be found in Table 4.1. The upper estimate for arteriole pulse pressure was extracted from Figure 2.2 as no exact value of this pressure variation was found. The same mean pressure and pulse pressure were used for the ICP and for the pressures in the PVS/ECS, as several studies have indicated that these pressures are largely similar [66, 67].

The clinical indicators in Table 4.1 govern the targeted behavior of the model. In addition, a total arterial blood flow into the brain must be established. This flow was extracted manually from the cerebral arterial flow curve in Figure 2.4, with the assumption that the cardiac cycle lasts one second in total. As such, a steady heart rate of 60 bpm was assumed throughout all simulations in this thesis. A graph illustrating this extracted arterial inflow can be seen in Figure 4.1, with the

Table 4.1: Clinical measurements and estimates that were used as indicators for the model.
* estimated since no value parameter was found in the literature

Parameter	Value	Unit	Reference
Mean arteriole pressure	50	mmHg	[42]
Mean venous pressure	$8.4 - 10$	mmHg	[42, 68]
Mean ICP pressure	10	mmHg	[69]
Arteriole-capillary pulse pressure	$4 - 10$	mmHg	[42, 70]
Venous pulse pressure	$0 - 0.1$	mmHg	*
ICP variation (temporal)	$3.5 - 7$	mmHg	[2, 11]
Peak transmantle pressure gradient	1.46 ± 0.74	$\frac{mmHg}{m}$	[11]
Peak displacement of tissue	$0.1 - 0.5$	mm	[38–40]
Aqueductal stroke volume	48 ± 223	μL	[1]
Peak aqueduct flow-rate	150	$\frac{\mu L}{s}$	[1]

same temporal resolution as used in the simulations.

Quantities of Interest   It is useful to have a way to compare the clinical indicators in Table 4.1 with the results of the simulations. Additionally, it is important to have a set of metrics that can be discussed and compared with results from other literature. Therefore, a set of expressions is established to describe the different quantities of interest. It should be noted that all the time-averaged values in this thesis use time intervals that start and end at the same point in the cardiac cycle. The pressures in the fluid networks are an important quantity for the verification of the model, as the range of values for these pressures is relatively well known. The spatially averaged fluid pressure in each network is defined as

$$p_{i,\text{avg}}(t) = \frac{1}{V} \int_{\Omega} p_i(t, x) dx \qquad (4.1)$$

with V being the volume of the domain Ω. Furthermore, $p_{i,\max}(t)$ and $p_{i,\min}(t)$ are defined as the maximal and minimal network pressures of the domain at time t, respectively. The pressures from the compartment model do not need special definitions, as they are zero-dimensional. The fluid velocity in the brain tissue also needs appropriate definitions. It is important to differentiate between the bulk flow of fluid described by the Darcy velocity in Equation (3.1), and the actual fluid velocities in the tissue. The average bulk flow velocity in network i is defined as

$$q_i(t) = \frac{1}{V} \int_{\Omega} || - K_i \nabla p_i(t, x)||_2 dx \qquad (4.2)$$
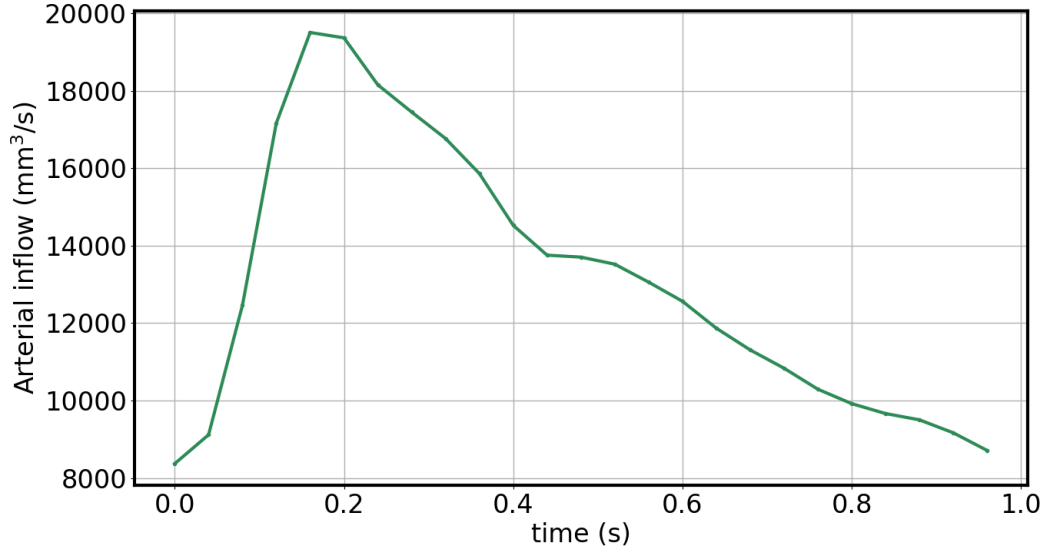
Figure 4.1: Illustration of the arterial flow curve used in the model. The flow curve was extracted manually from the cerebral arterial flow curve in Figure 2.4. The uniform source term g_1 in the model used this flow curve divided by the total volume of the simulation domain to ensure an equally large flow of blood.

where the expression inside the Euclidean norm is the Darcy velocity. The actual velocity of the fluid inside the tissue is likely to vary considerably depending on where the velocity is measured. Although an exact measure of such velocities is not possible in the current model, it is possible to give an estimate using by the porosity ϕ_i. Porosity is defined as the fraction of the volume of the fluid network compared to the total volume of brain tissue. This means that a lower porosity results in a higher fluid velocity because the bulk flow through the tissue is concentrated through a smaller volume. The estimate of the average fluid velocity in network i is specified as

$$v_i = \frac{q_i}{\phi_i} \tag{4.3}$$

The volume change and displacements of brain tissue are also of interest. The time derivatives of the volume change of the brain surfaces were defined in the previous chapter in Equations (3.19) and (3.20). Similarly, the relative change in surface volume is defined as

$$dV(t) = \int_\Gamma \boldsymbol{u}(t,x) \cdot \boldsymbol{n} ds - \frac{1}{\Delta t} \int^{\Delta t} \int_\Gamma \boldsymbol{u}(t,x) \cdot \boldsymbol{n} ds dt \tag{4.4}$$

with Γ denoting the surface boundary and Δt denoting a time interval from which a time-averaged surface expansion is calculated. Subtracting the average surface

expansion ensures that the relative surface expansion oscillates around zero instead of some arbitrary value. One reason for doing this is to have a direct measure of the variation in volume that the brain displaces. Another reason is that the arterial influx of blood will expand the volume of the brain before the ICP is raised sufficiently to resist further expansion. This net expansion generates large displacements that are not comparable to those in clinical studies, as these studies measure tissue displacements based on the relative motion of brain tissue[39, 71]. To estimate a displacement field comparable to those found in clinical studies, the displacements at the point in the cardiac cycle when total blood volume is minimized is obtained. This displacement field is then subtracted from the absolute displacement field so that the relative motion of the tissue can be calculated. The relative field of displacement, representing the pulsatile motion of tissue is defined as

$$U_r(x) = ||\boldsymbol{u}(x,t) - \boldsymbol{u}(x,t_r)|| \tag{4.5}$$

for all $x \in \Omega$ with t_r representing the point in the cardiac cycle at which the total blood volume is minimized.

4.2 Material Parameters for the MPET Model

An overview of the material parameters used in the MPET model for the brain parenchyma can be found in Table 4.2. Parameters such as density and viscosity do not vary significantly and are easily obtained. Other parameters are more uncertain and can vary by several orders of magnitude in different studies. These parameters values were typically chosen as a midrange value based on several studies or experimentally chosen based on replicating clinical measurements.

Biot-Willis Coefficient   Recall the expression for the total pressure in Equation (3.10). The expression is determined by the volumetric strain in the solid skeleton, as well as by a summation of all fluid pressures. Each fluid pressure is multiplied by an α known as the Biot-Willis coefficient. The α specifies how changes in fluid pressures transfer to stress in the solid matrix, and in the case of multiple network modeling, each individual α can be thought of as a weighting of how much each pore pressure contributes to normal stress in the porous matrix[80]. In the case of a single fluid network with an incompressible solid matrix, the Biot-Willis coefficient will have a value of $\alpha = 1$[81]. This value has been used in previous studies on the brain for single network models[82] as brain tissue is generally considered incompressible[83].

When modeling several fluid networks in the brain, the α for each individual network is highly uncertain. There are no previous clinical studies that relate these coefficients to the mechanical behavior of the brain, and the coefficients will change depending on how many networks are included in any given model.

Table 4.2: Base parameters used for the MPET component of the combined model.

* values that had to be estimated since no equivalent parameter was found in literature

** not the same value as in [72], but same decrease in order relative to the arteriole-venous transfer coefficient

Parameter	Value	Unit	Reference
ν, Poisson rate	0.49	-	[73]
E, Young Modulus	1.5	kPa	[43]
$\mu_{1,2}$, dynamic viscosity, blood	$2.67 \cdot 10^{-3}$	$Pa \cdot s$	[31]
μ_3, dynamic viscosity, CSF	$6.97 \cdot 10^{-4}$	$Pa \cdot s$	[24]
κ_1, arteriole permeability	10^{-10}	m^2	[31]
κ_2, venous permeability	10^{-10}	m^2	[31]
$\kappa_{3,p}$, permeability, PVS	10^{-10}	m^2	[72]
$\kappa_{3,e}$, permeability, ECS	10^{-14}	m^2	[74] [75]
S_1, arteriole storage coefficient	$4.47 \cdot 10^{-7}$	Pa^{-1}	[33]
S_2, venous storage coefficient	10^{-4}	Pa^{-1}	*
S_3, perivascular storage coefficient	$4.47 \cdot 10^{-7}$	Pa^{-1}	[33]
α_1, arteriole Biot-Willis coefficient	0.6	-	*
α_2, venous Biot-Willis coefficient	0.02	-	*
α_3, perivascular Biot-Willis coefficient	0.38	-	*
$\eta_{2\leftarrow1}$, arteriole-venous transfer	$1.75 \cdot 10^{-6}$	$Pa^{-1}s^{-1}$	*
$\eta_{2\leftarrow3}$, arteriole-paravascular transfer	$1.75 \cdot 10^{-7}$	$Pa^{-1}s^{-1}$	**[72]
$\eta_{2\leftarrow3}$, perivascular-venous transfer	$7.35 \cdot 10^{-6}$	$Pa^{-1}s^{-1}$	*
ϕ_1, arteriole porosity	$2.31 \cdot 10^{-3} - 1.09 \cdot 10^{-2}$	-	[76, 77]
ϕ_2, vein porosity	$1.09 \cdot 10^{-2} - 2.3 \cdot 10^{-2}$	-	[76, 77]
$\phi_{3,p}$, PVS porosity	$1.54 \cdot 10^{-3} - 4.04 \cdot 10^{-3}$	-	[78]
$\phi_{3,e}$, ECS porosity	$0.14 - 0.23$	-	[79]

A general requirement for the coefficients is that: $\phi \leq \alpha_j \leq 1$ for each individual fluid network j, where ϕ is the total porosity of the porous matrix[81, 84]. Furthermore, it is possible to demonstrate that the combined Biot-Willis coefficient of a porous material with multiple fluid networks can be written as a sum of the α of each individual network, if the material is assumed to be homogeneous on some larger scale[85]. Several more recent studies using MPET to model the brain parenchyma have used this relation to further constrain the combined Biot-Willis coefficient as: $\phi \leq \sum_{j=1}^{M} \alpha_j \leq 1$[28, 29, 31]. With the assumption that the combined Biot-Willis coefficient should be equal to one for an incompressible brain, the following constraint was used in this thesis

$$\sum_{j=1}^{M} \alpha_j = 1 \qquad (4.6)$$

for $M = 3$ total fluid networks. The contribution of each individual α_j to this summation had to be estimated based on some qualitative metric. Sobey & Wirth [86] showed that decreasing the Biot-Willis coefficient of the brain is equivalent to increasing its overall compliance. A decrease in α will decrease the load bearing effect of the parenchymal fluids, leading to an increase in solid strains, as the solid matrix must absorb a greater portion of the acting stress. This correlation between compliance and the Biot-Willis coefficient was used as a basis for estimating α_j of each individual network in this thesis. Their size was estimated based on their assumed compliance, with low-compliant networks having larger α and vice versa. Veins are characterized by higher compliance that dampens pulsatile blood flow compared to the arteries and arterioles. Veins are approximately 30 times more compliant than arteries[87, 88]. This ratio was used to estimate the difference between α_1 and α_2 for the arteriole and vein networks, respectively. Although this ratio characterizes the arteries and not the arterioles, it is argued that since the arteries are not represented as a network on its own, the arteriole network should aim to capture some of the mechanical contribution from the larger arteries. For the PVS/ECS network, compliance is highly uncertain and α_3 was chosen as a mid-range value between α_1 and α_2 while simultaneously maintaining the constraint in Equation (4.6).

Storage Capacity   The storage capacity of each fluid network is determined by the storage coefficient S_j. For a poroelastic brain model with a single fluid network representing ISF, the storage coefficient is the amount of ISF that can be forced into a fixed volume of parenchymal tissue under a unit increase in pore pressure [89, 90]. The storage coefficients describes both the storage capacity and the variation in pressure in each individual network. Therefore, it should be noted that the compliance of each network depends not only on the Biot-Willis coefficient but also on the storage coefficients. Unlike the Biot-Willis coefficient, storage capacity does not directly affect solid strains of the solid matrix. However, it does so indirectly, as small values for S lead to large temporal variations in pressure and

vice versa.

Although veins are more compliant than arteries and arterioles, their overall contribution to the volume change of parenchymal tissue is not necessarily greater due to small pressure pulsations. Veins contain approximately 70 % of total blood volume and are associated with small changes in venous pressure[91]. Large blood volume and small changes in pressure can be obtained by a (relatively) large storage coefficient. While estimates of this coefficient exist from previous MPET studies, preliminary tests showed that most of these previous studies underestimated its size when including pulsatility. These estimates yielded large temporal variations in venous pressure, which were not captured in these earlier studies, since pulsatility was not included. In this thesis, the coefficient was estimated on the basis of obtaining negligible small temporal pressure variations.

Similarly, the storage coefficients for the arteriole network and PVS/ECS had to be much smaller than for the venous network in order to facilitate small fluid volumes and large instantaneous variations in pressure. The estimate of these coefficients from Chou et al. [33] was found to be low enough to induce sufficiently high pressure variations, corresponding to the pulse pressures listed in Table 4.1.

MPET Transfer Coefficients   The transfer coefficients $\eta_{i \leftarrow j}$ in the linear transfer terms in the MPET equations quantifies the resistance of flow from one network to another. In the case of modeling fluid networks in biological tissue, these coefficients must often be estimated based on the specific characteristics of the modeled networks. As explained in the previous chapter, it is assumed that all fluid entering the arteriole network is transferred to the venous network or to the PVS and is not allowed to exit through other routes. The following relation was used to estimate the transfer coefficient between the arteriole and the venous network

$$\eta_{2 \leftarrow 1} = \frac{G_1}{\Delta P_{12} V}$$

in which G_1 is the mean arterial flow during each cardiac cycle, V is the volume of the modeled brain, and ΔP_{12} is the pressure drop between the arteriole and the venous network. This relation follows directly by applying mass conservation to the MPET system when a zero flux boundary condition is specified for the arteriole network and assuming that fluid transfer from the arteriole to the perivascular network is negligible compared to blood flow. The assumed pressure drop was estimated as the difference between the mean arteriole and the (lower) mean venous pressure in Table 4.1. The mean arterial blood flow into the arteriole network was specified to be: $688 \frac{\text{mL}}{\text{min}}$ for a healthy individual according to Baledént [1]. With the modeled brain having a total volume of 1173.67mL, the resulting transfer coefficient was estimated.

No clinical estimate of the transfer coefficient between the arteriole network and the PVS was found. Therefore, it was specified to be one order of magnitude lower than the arteriole to venous transfer coefficient, same as in one of the earlier MPET studies on pulsatility[72]. That study did not include any transfer term between the PVS and the venous network, which was needed in this model. Through arterial bloodflow, CSF is accumulated in the PVS and the CSF-filled cavities in the compartment model. To maintain a sufficient pressure drop between the arteriole network and the PVS network, accumulated CSF must be drained through some additional route. If not, the pressure in the PVS would rise to the same level as the arteriole network and then be drained trough the venous network from there. Instead, a direct drainage route through the venous network was added for the PVS network. This transfer coefficient was estimated the same was as the transfer coefficient between the arteriole and venous network

$$\eta_{2\leftarrow 3} = \frac{G_3}{\Delta P_{32} V}$$

with G_3 being the assumed rate of accumulated CSF/ISF, estimated to be one order of magnitude lower than G_1. With an assumed pressure drop of 1mmHg between the PVS and the vein network, the transfer coefficient was estimated.

Lamè constants   Young's modulus will vary naturally due to variations in the type of tissue contained in the brain. Typically, we differentiate between two types of tissues; white and grey matter. The outer layer of the brain is composed of gray matter, and the inner core is made up of white matter. [43] For this thesis a middle value between the two types of tissues were chosen for the Young modulus. The Lamè constants from the governing equations are related to the Poisson ratio and the Young modulus by the following equations

$$\lambda = \frac{\nu E}{(1+\nu)(1-2\nu)} \tag{4.7a}$$

$$\mu = \frac{E}{2(1+\nu)} \tag{4.7b}$$

$$\tag{4.7c}$$

Porosity Coefficients   The porosity coefficients for the different fluid networks are not used for the calculations of the MPET model, but are used for estimates of fluid network velocities, governed by Equation (4.3). Instead of specifying a single porosity for each network, a range of values will be specified, which will be used for discussions and comparisons with similar velocities from the literature. The porosities of the different networks are summarized at the bottom of Table 4.2.

The porosity of the arteriole/capillary network will vary significantly based on the assumed size of this network. No direct estimate was found for the porosity of

the cerebral arterioles, and estimates of porosities for cerebral arteries are instead used as an upper estimate. Similarly, estimates of cerebral capillary porosity can be used as a lower estimate of this network. The porosity of the PVS is highly uncertain and no direct measure of the value exists. In this thesis, the value was estimated based on a range of measurements of total PVS volumes by Ballerini et al. [78], divided by the total volume of the computational domain used in the model.

4.3 Material Parameters: Boundary Conditions and Compartment Model

A summary of the various parameters used to model the compartment model and the boundary conditions for the MPET model is found in Table 4.3. Estimated values and uncertain parameters are also discussed in this section.

Boundary Permeability   The β parameter, used for the boundary conditions of the ECS network, describes how permeable the boundaries of the brain parenchyma are. When quantifying the exchange of CSF with the ECS, the parameter can be explained by a combination of two factors. The first is the permeability and thickness of the membranes that separate the CSF-filled cavities and the brain parenchyma. On the outer surface of the brain, the pia mater (pia) separates the cerebral cortex from the SAS, while on the inner ventricle surface, the ependyma separates the brain tissue from the CSF[92]. Since the pia membrane is generally considered to have a very low permeability[93], a more likely factor explaining this parameter could be the drainage rate through perivascular spaces and into the ECS.

Only a few studies have attempted to estimate the resistance to flow from CSF-filled cavities to ECS. Flow resistance from perivascular spaces to the ECS has been calculated [68], while only the elastic properties of the pia have been measured [94]. Levine [89] investigated the role of the brain parenchyma in absorbing CSF, in relation to normal pressure hydrocephalus (NPH) and showed that some CSF seepage through the ventricle wall explained the clinical characteristics of NPH. He assumed that the permeability of the pia and ependyma was the same as that of the brain parenchyma, which was also assumed in this thesis to model the third fluid network as a PVS. This essentially means that fluid is exchanged freely between the PVS and CSF-filled cavities and that the only resistance to this exchange is the permeability of the PVS network itself. When the third fluid network is modeled as an ECS, a small additional resistance of $\beta = 0.1$ is added to quantify the assumed resistance that the CSF first flows into perivascular spaces, before being exchanged with the ISF in the ECS.

Relative Ventricular Pressure   The additional compliance of the ventricle compartment facilitates a transmantle pressure gradient between the SAS and the

Table 4.3: Model parameters used for the compartment model and the boundary conditions of the MPET domain.
** article specifies values in the range of $5-15$mmHg for healthy adults

Parameter	Value	Unit	Reference
Intracranial Pressure, ICP			
PVI (pressure-volume index)	7.36	mL	[51]
P_b (baseline pressure, ICP)	10	mmHg	**[69]
Relative ventricular pressure, P_R			
C, ventricle (additional) compliance	0.0412	$\frac{mL}{Pa}$	*
d, aqueductal diameter	4	mm	[95]
L, aqueductal lenght	70	mm	[95]
R_{AQ}, aqueductal resistance	7.77	$\frac{Pa \cdot s}{mL}$	*
Venous back-pressure			
P_{VEIN}	8.4	mmHg	[68]
Boundary permeability, ECS			
β	0.1	-	*

ventricles. The following relation was used to estimate this compliance

$$C = \frac{\Delta V}{\Delta P}$$

in which ΔV is the maximal assumed volume change from some reference volume, and ΔP is the corresponding pressure change. For the ventricle, this volume change is assumed to correspond to the aqueductal stroke volume. To estimate the corresponding change in pressure, the resistance of the cerebral aqueduct is first introduced. The aqueductal flow is simplified as a Poiseuille flow, assuming laminar flow through a rigid pipe. The flow resistance can then be estimated as

$$R_{AQ} = \frac{128L\mu_f}{\pi d^4}$$

where d and L represent an effective diameter and length of the aqueduct, respectively[95]. μ_f is the dynamic fluid viscosity of the ventricular CSF and has the same value as the CSF/ISF in the fluid networks. The pressure change corresponding to the maximal volume change is then estimated as

$$\Delta P = Q_p R_{AQ}$$

where Q_p is the peak aqueductal flow rate, listed in Table 4.1

Chapter 5

Numerical Methods

The combined model in this thesis applies a partitioned approach for solving the complete system of equations. This means that the system of MPET equations and the compartment model are solved separately rather than as a single system of equations. Each component takes turns of being solved, and the coupling between the two components terms are imposed at each turn. In this chapter, the variational formulation of the MPET system is presented, along with a mixed FEM to solve the discretized problem. After that, a coupled numerical algorithm is introduced that solves the combined intracranial model. In addition, an overview of the various geometries and meshes used for the simulations is presented, along with the numerical framework used to implement the model.

5.1 Variational formulation of the Poroelasticity Problem

The governing equations in (3.13) need to be formulated in its weak form in order to solve the system using a mixed-FEM. A set of function spaces is defined for displacements u, total pressure p_0 and for the three fluid pressures p_1, p_2, and p_3. Consider the poroelastic domain. of $\Omega \subset \mathbb{R}^3$. A Hilbert space $L^2(\Omega)$ is introduced, defining a set of square-integrable real-valued functions on Ω. This means that for every $f \in L^2$ the following relation holds true

$$\int_\Omega f^2 dx < \infty$$

The notation $\langle f, g \rangle$ is used to denote the inner product of $L^2(\Omega)$ and is defined as

$$\langle f, g \rangle = \int_\Omega f g \, dx$$

and the notation $\langle f, g \rangle_\Gamma$ is used to denote the inner product on the boundary $\Gamma \subset \partial\Omega$ defined as

$$\langle f, g \rangle_\Gamma = \int_\Gamma f g \, ds$$

The first-order Sobolev space of $H^1(\Omega)$ consists of a set of functions $f \in L^2(\Omega)$ where the weak first-order derivatives of f exist in all three spatial dimensions. Additionally, $H^1_{0,\Gamma} \subset H^1$ is a subset that consists of the functions $f \in H^1$ at which the trace is zero on the boundary such that $f(x) = 0$ on $\Gamma \subset \partial\Omega$. [72] When $\Gamma = \partial\Omega$ this notation is simplified to H^1_0. The zero-trace condition is necessary on all Dirichlet boundaries. It essentially ensures that the function being solved is not defined on these boundaries and is instead imposed directly through the boundary condition.

To account for temporal derivatives, the time interval $t \in [0, T]$ is considered with a set of continuous differentiable functions $f : [0, T] \mapsto H^1(\Omega)$ denoted as $C^1([0, T], H^1(\Omega)) = \{f \,|\, \frac{\partial f}{\partial t} \in C^0([0, T]; H^1)\}$ which implies that the first-order temporal derivative of f exists in H^1, in a weak sense.
For further derivations, the following function spaces are defined

$$\boldsymbol{V} = H^1(\Omega; \mathbb{R}^3), \;\; Q_0 = L^2, \;\; Q_1 = H^1 \;\; Q_2 = H^1_{0,\Gamma_{\text{SAS}}} \;\; Q_3 = H^1_0 \tag{5.1}$$

The variational formulation of the problem arises by multiplying the governing equations in (3.13) by sufficiently smooth test functions in the respective function spaces. Applying the inner product and using Green's Theorem for second-order derivatives yields the following variational problem: find $\boldsymbol{u} \in C^1([0, T]; \boldsymbol{V})$ and $p_i \in C^1([0, T]; Q_i)$ for $i = 0, 1, 2, 3$ such that

$$\langle 2\mu\epsilon(\boldsymbol{u}), \epsilon(\boldsymbol{v})\rangle + \langle p_0, \text{div}\,\boldsymbol{v}\rangle = \langle \boldsymbol{\sigma} \cdot \boldsymbol{n}, \boldsymbol{v}\rangle_{\partial\Omega} \quad \forall \boldsymbol{v} \in \boldsymbol{V} \tag{5.2a}$$

$$\langle \text{div}\,\boldsymbol{u}, q_0\rangle - \langle \lambda^{-1}\alpha \cdot p, q_0\rangle = 0 \qquad\qquad \forall q_0 \in Q_0 \tag{5.2b}$$

$$\langle S_1\dot{p}_1 + \alpha_1\lambda^{-1}\alpha \cdot \dot{p} + \gamma_1, q_1\rangle + \langle K_1\nabla p_1, \nabla q_1\rangle = \langle g_1, q_1\rangle \qquad \forall q_1 \in Q_1 \tag{5.2c}$$

$$\langle S_2\dot{p}_2 + \alpha_2\lambda^{-1}\alpha \cdot \dot{p} + \gamma_2, q_2\rangle + \langle K_2\nabla p_2, \nabla q_2\rangle = 0 \qquad \forall q_2 \in Q_2 \tag{5.2d}$$

$$\langle S_3\dot{p}_3 + \alpha_3\lambda^{-1}\alpha \cdot \dot{p} + \gamma_3, q_3\rangle + \langle K_3\nabla p_3, \nabla q_3\rangle = 0 \qquad \forall q_3 \in Q_3 \tag{5.2e}$$

with the surface integral for the momentum Equation (5.2b) defined as

$$\langle \boldsymbol{\sigma} \cdot \boldsymbol{n}, \boldsymbol{v}\rangle_{\partial\Omega} = \langle P_{\text{SAS}}\boldsymbol{n}, \boldsymbol{v}\rangle_{\Gamma_{\text{SAS}}} + \langle P_{\text{VEN}}\boldsymbol{n}, \boldsymbol{v}\rangle_{\Gamma_{\text{VEN}}}$$

An additional formulation is needed to model the third fluid network as an ECS, owing to its Robin boundary conditions. With the function space for the pressure now defined as: $Q_3 = H^1$, the variation formulation for Equation (5.2e) instead becomes

$$\langle S_3\dot{p}_3 + \alpha_3\lambda^{-1}\alpha \cdot \dot{p} + \gamma_3, q_3\rangle + \langle K_3\nabla p_3, \nabla q_3\rangle = \langle K_3\nabla p_3 \cdot \boldsymbol{n}, q_3\rangle_{\partial\Omega} \;\; \forall q_3 \in Q_3 \tag{5.3}$$

with the surface integral on the right-hand side defined as

$$\langle K_3 \nabla p_3 \cdot \boldsymbol{n}, q_3 \rangle_{\partial\Omega} = \langle \beta(P_{\text{SAS}} - p_3), q_3 \rangle_{\Gamma_{\text{SAS}}} + \langle \beta(P_{\text{VEN}} - p_3), q_3 \rangle_{\Gamma_{\text{VEN}}}$$

5.2 Mixed Finite Element Formulation

To formulate a mixed finite element problem of the variational formulation in (5.2), the Galerkin method for differential equations is applied. The method involves enforcing that the residual of each function is orthogonal to its respective function space[62]. A mesh discretization of conforming tetrahedral elements $\{\mathcal{T}_h\}_{h>0}$ onto Ω is considered, with h denoting the characteristic size of the mesh elements. The generic discrete spaces of $\boldsymbol{V}_h \subset \boldsymbol{V}$ and $Q_{i,h} \subset Q_i$, $i = 0, 1, 2, 3$ are considered. Furthermore, an implicit Euler discretization in time is employed, defining N discrete time points as: $0 = t_0 < t_1 < ... < t_N = T$ for a final time T. The time step for the implicit scheme is then defined as $\tau_n = t_n - t_{n-1}$. In addition, a discrete time differential δ_t is utilized as

$$\delta_t p_h^n = \frac{p_h^n - p_h^{n-1}}{\tau_n}$$

The Galerkin scheme is formulated similarly as in Oyarzùa et al. [59] and reads as follows: Find $\boldsymbol{u}_h^n \in \boldsymbol{V}_h$, and $p_{i,h}^n \in Q_{i,h}$, $i = 0, 1, 2, 3$ for all $n \in 1, 2, ..., N$ such that

$$\langle 2\mu\boldsymbol{\epsilon}(\boldsymbol{u}^N), \boldsymbol{\epsilon}(\boldsymbol{v}) \rangle + \langle p_0^n, \text{div } \boldsymbol{v} \rangle = \langle \boldsymbol{\sigma}^n \cdot \boldsymbol{n}, \boldsymbol{v} \rangle_{\partial\Omega} \quad \forall \boldsymbol{v} \in \boldsymbol{V}_h \tag{5.4a}$$

$$\langle \text{div } \boldsymbol{u}^n, q_0 \rangle - \langle \lambda^{-1}\alpha \cdot p^n, q_0 \rangle = 0 \qquad \forall q_0 \in Q_{0,h} \tag{5.4b}$$

$$\langle S_1 \delta_t p_1^n + \alpha_1 \lambda^{-1}\alpha \cdot \delta_t p^n + \gamma_1^n, q_1 \rangle + \langle K_1 \nabla p_1^n, \nabla q_1 \rangle = \langle g_1^n, q_1 \rangle \qquad \forall q_1 \in Q_{1,h} \tag{5.4c}$$

$$\langle S_2 \delta_t p_2^n + \alpha_2 \lambda^{-1}\alpha \cdot \delta_t p^n + \gamma_2^n, q_2 \rangle + \langle K_2 \nabla p_2^n, \nabla q_2 \rangle = 0 \qquad \forall q_2 \in Q_{2,h} \tag{5.4d}$$

$$\langle S_3 \delta_t p_3^n + \alpha_3 \lambda^{-1}\alpha \cdot \delta_t p^n + \gamma_3^n, q_3 \rangle + \langle K_3 \nabla p_3^n, \nabla q_3 \rangle = 0 \qquad \forall q_3 \in Q_{3,h} \tag{5.4e}$$

in which the lower index h of the discrete test and trial functions has been dropped for readability. Similarly to the variational formulation, the stress acting on the boundaries in Equation (5.4b) is defined as

$$\langle \boldsymbol{\sigma}^n \cdot \boldsymbol{n}, \boldsymbol{v} \rangle_{\partial\Omega} = \langle P_{\text{SAS}}^{n^*}\boldsymbol{n}, \boldsymbol{v} \rangle_{\Gamma_{\text{SAS}}} + \langle P_{\text{VEN}}^{n^*}\boldsymbol{n}, \boldsymbol{v} \rangle_{\Gamma_{\text{VEN}}}$$

and the alternative formulation for the third fluid network modeled as an ECS is specified, with the right-hand side in Equation (5.4e) now defined as

$$\langle K_3 \nabla p_3^n \cdot n, q_3 \rangle_{\partial\Omega} = \langle \beta(P_{\text{SAS}}^{n^*} - p_3^n), q_3 \rangle_{\Gamma_{\text{SAS}}} + \langle \beta(P_{\text{VEN}}^{n^*} - p_3^n), q_3 \rangle_{\Gamma_{\text{VEN}}}$$

while for the PVS, the boundary pressures are given directly to the solution through the Dirichlet condition. With this formulation, the solution is solved at each discrete time point t_n. It should be noted that arterial inflow modeled by the source term g_1^n is explicitly provided at each iteration. Similarly, the venous back pressure on the boundary is constant and therefore also defined for all time points. In contrast, the boundary pressures $P_{\text{SAS}}^{n^*}$ and $P_{\text{SAS}}^{n^*}$ must be solved in-between each time point, using the compartment model described in Chapter 3. The notation n^* is used to emphasize that the compartment pressure at t^{n^*} is applied to the model at the current time t^n, but is counted with an index lower, i.e. $n^* = n - 1$ for all $t^n \in t^1, t^2, ..., t^N$

5.3 Coupled Numerical Algorithm

In this section, a complete overview of the coupled numerical algorithm for the combined model is given. A flow chart illustrating the order of algorithm is shown in Figure 5.1. To start, the initial conditions for the mixed-FEM in (5.4) and for the ICP of the compartment model are defined to be

$$\boldsymbol{u}^0 = 0 \quad p_1^0 = P_{1,\text{mean}} \quad p_2^0 = P_{\text{VEIN}} \quad p_3^0 = P_b \quad P_{\text{SAS}}^{0^*} = P_{\text{VEN}}^{0^*} = P_b \tag{5.5}$$

where the initial values for the displacements and poroelastic pressures are applied uniformly on the discretized domain. $P_{1,\text{mean}}$ is the assumed mean pressure defined in Table 4.1. P_{VEIN} and P_b are the venous back pressure and the baseline ICP pressure, respectively, and are both defined in Table 4.3. After solving an iteration for the mixed-FEM at time t^n, the pressures in the compartment model must be calculated. Recall the expressions for the ICP and the ICPV in Chapter 3. Both pressures are functions of the surface expansion and outflow of CSF from the poroelastic domain, defined in Equations (3.19) to (3.22). The surface integrals of the wall displacements are calculated as

$$V_{\text{SAS}}^n = \int_{\Gamma_{\text{SAS}}} \boldsymbol{u}^n \cdot \boldsymbol{n} ds \tag{5.6}$$

$$V_{\text{VEN}}^n = \int_{\Gamma_{\text{VEN}}} \boldsymbol{u}^n \cdot \boldsymbol{n} ds \tag{5.7}$$

The time derivatives of the wall displacements, which quantify the relative change in parenchymal volume, are then defined to be

$$\dot{V}_{\text{SAS}}^{n^*} = \tau_n^{-1}(V_{\text{SAS}}^n - V_{\text{SAS}}^{n-1}) \tag{5.8}$$

$$\dot{V}_{\text{VEN}}^{n^*} = \tau_n^{-1}(V_{\text{VEN}}^n - V_{\text{VEN}}^{n-1}\tau_n) \tag{5.9}$$
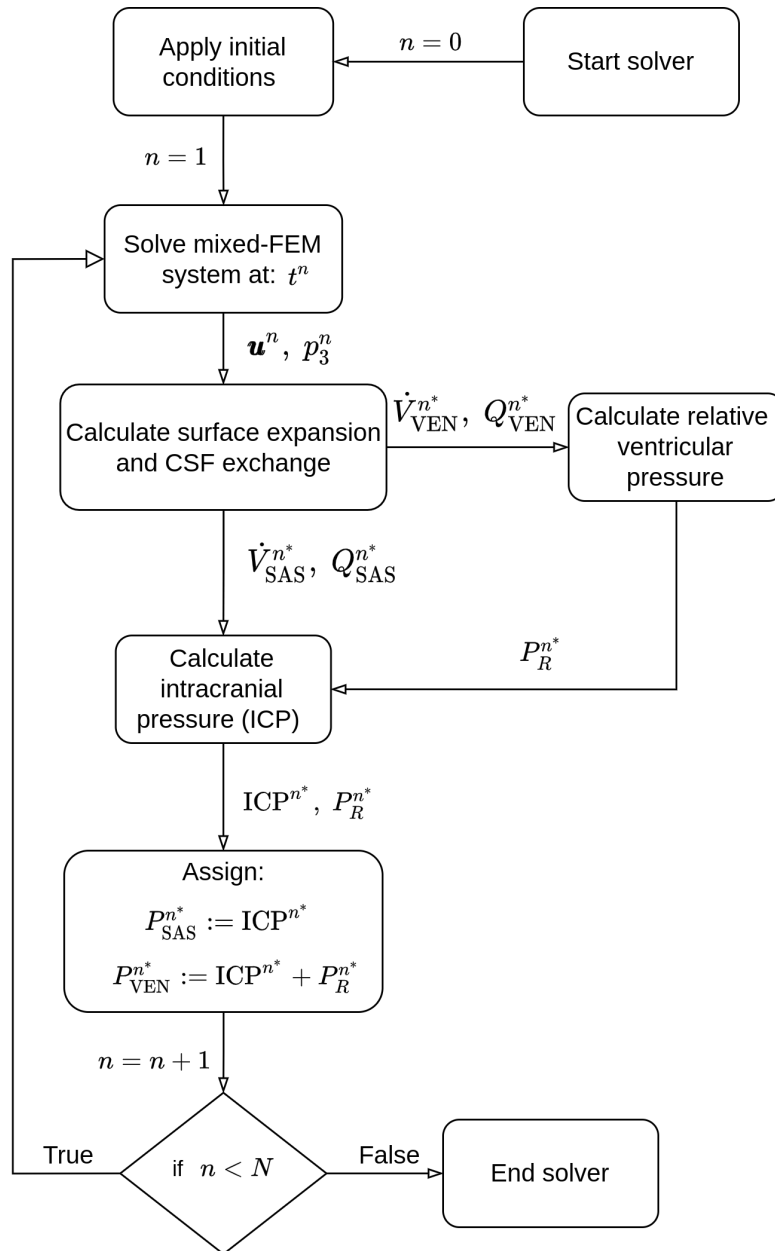
Figure 5.1: Overview of the solver used in this thesis. The flowchart illustrates the order of which the different components are calculated. The different variables next to the arrows indicate which quantities that are used to solve the different steps.

In addition, the CSF exchange rates between the PVS/ECS and the CSF filled cavities are calculated as

$$Q_{\text{SAS}}^{n^*} = \int_{\Gamma_{\text{SAS}}} -K_3 \nabla p_3^n \cdot \boldsymbol{n} ds \qquad (5.10)$$

$$Q_{\text{VEN}}^{n^*} = \int_{\Gamma \text{VEN}} -K_3 \nabla p_3^n \cdot \boldsymbol{n} ds \qquad (5.11)$$

Since the ICP depends on the aqueductal flow rate, the relative ventricular pressure is calculated first. Using implicit Euler for Equations (3.17) and (3.18) yields

$$P_R^{n^*} = \frac{\tau_n(\dot{V}_{\text{VEN}}^{n^*} + Q_{\text{VEN}}^{n^*}) + C P_R^{(n-1)^*}}{C + \tau_n R_{\text{AQ}}^{-1}} \qquad (5.12)$$

with the current aqueductal flow rate specified as: $Q_{\text{AQ}}^{n^*} = -\frac{P_R^{n^*}}{R_{\text{AQ}}}$. The change in intracranial volume, defined in Equation (3.15) is then calculated as

$$\Delta V^{n^*} = \Delta V^{(n-1)^*} + \tau_n(Q_{\text{SAS}}^{n^*} + \dot{V}_{\text{SAS}}^{n^*} - Q_{\text{AQ}}^{n^*}) \qquad (5.13)$$

and finally, the ICP can be calculated as

$$\text{ICP}^{n^*} = P_b \cdot 10^{\Delta V^{n^*}/\text{PVI}} \qquad (5.14)$$

The pressure acting on the boundaries of the SAS and the ventricles are then assigned the respective values

$$P_{\text{SAS}}^{n^*} := \text{ICP}^{n^*}$$

$$P_{\text{VEN}}^{n^*} := \text{ICP}^{n^*} + P_R^{n^*}$$

which are in turn used to solve the poroelastic problem at the next time point: t^{n+1}.

5.4 Numerical Implementation

The code developed for the solver can be found at: https://github.com/AasmundResell/MPET-modelling

The solver for the mixed FEM in 5.4 was implemented using FEniCS, which is an open-source software tailored for solving a wide range of PDE's using FEM. The software provides a framework in Python for easily generating efficient c++ code with a level of abstraction that is close to the variational formulation of the problem. All other calculations were made with the mathematical Python library: Numpy.

A short example for solving a PDE in its weak form using FEniCS is provided in the following section. Consider the standard problem of linear elasticity for which

small deformations are assumed. A simple 2-dimensional domain is considered: $\Omega = [0, 10] \times [0, 3]$ The governing equations of the problem reads

$$-\nabla \cdot \boldsymbol{\sigma} = \boldsymbol{f} \quad \text{in} \quad \Omega \qquad (5.15a)$$

$$\boldsymbol{\sigma}(\boldsymbol{\varepsilon}) = 2\mu\boldsymbol{\varepsilon} + \lambda tr(\boldsymbol{\varepsilon})\boldsymbol{I} \qquad (5.15b)$$

$$\boldsymbol{\varepsilon}(\boldsymbol{u}) = \frac{1}{2}(\nabla\boldsymbol{u} + (\nabla\boldsymbol{u})^{\mathsf{T}}) \qquad (5.15c)$$

in which $\boldsymbol{\varepsilon}$ is the small strain tensor, $\boldsymbol{\sigma}$ is the stress tensor and $\boldsymbol{f} = [0, \rho g]$ is the force acting downward on a unit volume, with $g = -9.81\frac{m}{s}$ and $\rho = 1\frac{kg}{m}$. $\mu = 1$Pa and $\lambda = 1$Pa are the standard Lamé elasticity parameters. In this problem, the domain Ω is considered as a simple beam which is clamped on the left side. In addition to the gravitational force, a traction force acts downward on the right side of the beam and is defined as: $\boldsymbol{T} = [0, 10]$.

To formulate a variational formulation, the governing equation is multiplied by a test function $\boldsymbol{v} \in \hat{V}$ in which $\hat{V}$ is a vector-valued function space. By applying the inner product over the domain Ω and using integration by parts on second-order derivatives, the weak form of the problem in Equation (5.15) is formulated as

$$\int_{\Omega} \boldsymbol{\sigma}(\boldsymbol{u}) : \boldsymbol{\varepsilon}(\boldsymbol{v})dx = \int_{\Omega} \boldsymbol{f} \cdot \boldsymbol{v}dx + \int_{\partial\Omega_N} (\boldsymbol{\sigma}(\boldsymbol{u}) \cdot \boldsymbol{n})ds \qquad (5.16)$$

in which the gradient $\nabla\boldsymbol{v}$ has been replaced by the symmetric tensor $\boldsymbol{\varepsilon}(\boldsymbol{v})$ which can be shown to hold true because $\boldsymbol{\sigma}(\boldsymbol{u})$ is symmetric. The traction force $\boldsymbol{T} = \boldsymbol{\sigma} \cdot \boldsymbol{n}$ on the right boundary is enforced by a natural Neumann boundary condition. An implementation of the specified problem above is given on the next page, illustrating how the problem can be solved using FEniCS with a relatively short and compact code.

Code listing 5.1: Python example from file

```python
from fenics import *

mu = 1
lambda_ = 1
rho = 1
g = 9.81

x0, y0 = 0.0, 0.0
x1, y1 = 10.0, 3.0
nx = 20
ny = 6

mesh = RectangleMesh(Point(x0, y0), Point(x1, y1), nx, ny)

V = VectorFunctionSpace(mesh, "Lagrange", 2)

# Checks for clamped boundary
def clamped_boundary(x, on_boundary):
    tol = 1e-14
    return on_boundary and x[0] < tol

# Defines the Diriclet boundary condition
bc = DirichletBC(V, Constant((0, 0)), clamped_boundary)

# Functions for stress and strain tensors
def epsilon(u):
    return 0.5 * (nabla_grad(u) + nabla_grad(u).T)

def sigma(u):
    return lambda_ * nabla_grad(u) * Identity(d) + 2 * mu * epsilon(u)

#  Variational problem
u_ = TrialFunction(V)
v = TestFunction(V)
d = u_.geometric_dimension()
f = Constant((0, -rho * g))
T = Constant((0, 10))
a = inner(sigma(u_), epsilon(v)) * dx
L = dot(f, v) * dx + dot(T, v) * ds

# Compute solution
u = Function(V)
solve(a == L, u, bc)
```

5.5   Meshes and Numerical Accuracy

The finite elements of the model used continuous Galerkin elements (CG) for the calculations in FEniCS. The total pressure and the pressures of the fluid networks used first-order polynomials, whereas the displacements used second-order polynomials. Using polynomials of one degree higher order for displacements compared to pressure is a necessary condition to obtain optimal convergence rates with this type of system[72, 96]. It is also noted that for the calculation of the CSF exchange in Equations (5.10) and (5.11), the Darcy-velocity field was projected

Table 5.1: Statistics for the different meshes used in the mesh sensitivity study. The system size is the size of the system matrix.

Mesh	Number of elements	Number of vertices	System size
Sphere mesh			
N = 13	5070	1061	27326 × 27326
N = 15	7471	1507	39000 × 39000
N = 17	11339	2209	58600 × 58600
N = 20	17993	3409	91468 × 91468

one order higher, which has been shown to raise the numerical accuracy[97]. A summary of the different mesh statistics is listed in Table 5.1. The geometry of the idealized sphere used a ratio between the inner and outer radius as: $\frac{r_i}{r_o} = 0.3$, similar to several previous studies that used this idealized geometry to model the brain[34, 89, 98]. The inner and outer radius of the sphere were scaled to fit a realistic volume of the brain, resulting in an inner radius of $r_i = 19.81$mm and an outer radius of $r_o = 66.04$mm.

A sensitivity study of spatial mesh discretization was conducted with this geometry. The study investigated the effect on mass conservation between the various fluid networks by assessing the total size of the transfer terms. These terms were considered since their numerical accuracy is reliable for first-order pressure elements regardless of mesh sizes[97]. Additionally, assessing the mass conservation between fluid networks provides a clear metric to compare the different mesh refinements. The mesh sizes were defined by a division parameter N, which (approximately) discretized the geometry over the diameter of the sphere N times, resulting in a characteristic mesh size of $h = \frac{2r_o}{N}$. A cut of this mesh is shown in Figure 5.2, with a division parameter of $N = 13$.
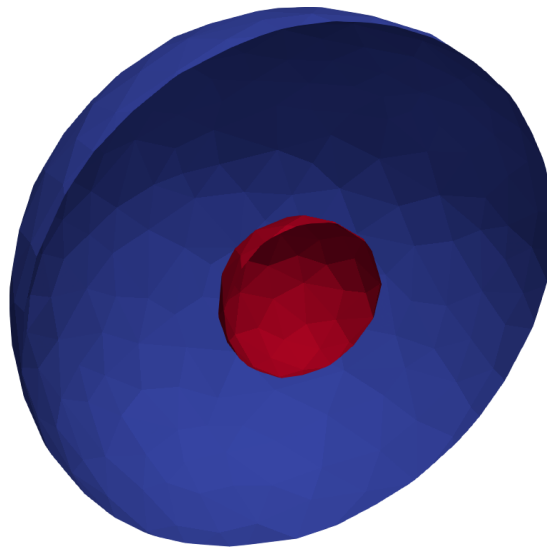
Figure 5.2: Half cut of the mesh of the idealized sphere geometry. Red indicates the inner boundary of the ventricles, while blue represents the outer boundary of the SAS. The inner facets and edges are removed in this illustration.

Chapter 6

Results

In this chapter, the results of this thesis are presented. First, the results of the physical simulations are presented in detail, with an emphasis on important quantities of interest. All results are reported after a periodic steady state solution is obtained. Furthermore, significant variations are reported for the alternative modeling configurations described in Table 3.2. In addition, the results of the sensitivity study are presented and significant variations between the different mesh refinements are reported.

6.1 Pressure Distribution

Plots of the temporal pressure variation in the arteriole network and the vein network for the standard PVS configuration are shown in Figure 6.1 during a single cardiac cycle. The arteriole network obtained a time-averaged fluid pressure of 53.63 mmHg and a peak value of 55.68 mmHg, found at $\Delta t_a = 0.4$ s. Here, Δt_a has been defined to denote the time that has passed after the minimal influx of arterial blood (see Figure 4.1 for reference) and can also be considered as a measure of the time passed after the beginning of the cardiac cycle. The pulse pressure amplitude of the different networks was calculated as the maximal temporal difference of the mean pressure, which was defined in Equation (4.1). This value was calculated to be 5.06 mmHg for the arteriole network. The spatial variation in the arteriole network was small compared to the temporal variation, which is illustrated by the pressure curves in Figure 6.1a, and also by the contour plots of the spatial variation of pressure in the blood networks, shown in Figure 6.2. Plots from the standard PVS configuration are located on the left side, and the equivalent plots for the ECS configuration are located on the right side. The arteriole network of the standard configuration had a slightly higher pressure on the ventricle wall than on the cortical surface at all time steps, as illustrated by Figures 6.2a and 6.2c. In comparison, the ECS configuration that has lower permeability and additional resistance at the boundary had more spatial variation in pressure, as illustrated by Figures 6.2b and 6.2d.
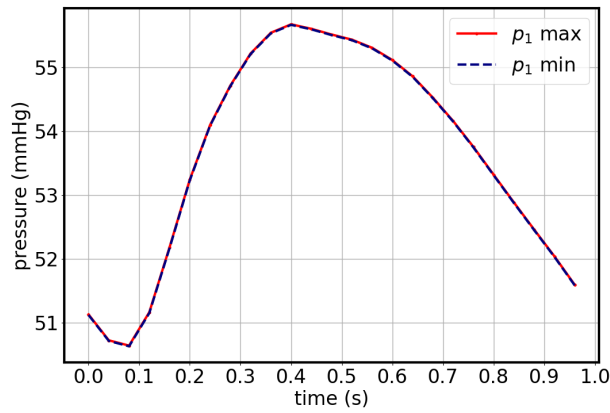
(a) Maximal and minimal arteriole pressures
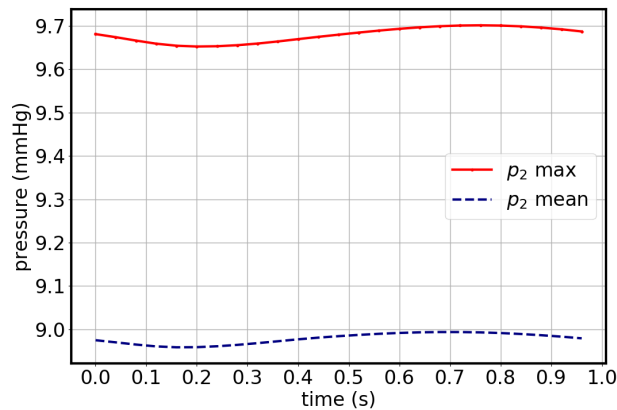
(b) Maximal and mean vein pressures

Figure 6.1: Plots of blood network pressures during one cardiac cycle. The plots illustrates: (a) the maximal and minimal pressure of the arteriole/capillary fluid network, (b) the maximal and mean fluid pressure of the vein network. The minimal vein is not included as it was constant and equal to the venous back-pressure. Both plots are extracted from the standard PVS configuration after 44 seconds of simulation time.

The pressure of the venous network had a negligible difference between the standard PVS configuration and the ECS configuration. For these two configurations, the vein pressure had an average value over time of 8.98 mmHg and peak values of 9.70 mmHg. The vein pressure was characterized by small temporal variations that resulted in a nearly flat pressure curve, as seen in Figure 6.1b. Spatial variance was significantly higher in the venous network compared to the other networks, as illustrated in Figures 6.2e and 6.2f. The largest spatial difference in venous pressure was found to be 1.3 mmHg for the standard PVS configuration and the

ECS configuration with the maximal value located on the ventricle wall. The minimal vein pressure was constant and equal to the venous back-pressure applied on the cortical surface.

The minimum ICP value of the standard PVS configuration was obtained at the beginning of the cardiac cycle and calculated as 8.21 mmHg. ICP increased rapidly during the early stage of the cardiac cycle, following the increase in arterial blood volume before reaching a peak value of 11.46 mmHg, resulting in a maximum temporal variation of 3.25 mmHg. The maximal ICP was found at $\Delta t_a = 0.4$ s. The average ICP was calculated to be 10.06 mmHg. A plot of the ICP along with the mean PVS pressure is shown in Figure 6.3a.

A slower decrease in ICP followed during the diastolic phase until the beginning of the next cardiac cycle. The relative ventricular pressure P_R that represents the spatial variation of the ICP is shown in Figure 6.3c for the standard PVS configuration. The relative pressure had a time-averaged value of 0.37Pa with peaks of 1.30Pa. This resulted in a peak spatial ICP gradient of $0.21 \frac{\text{mmHg}}{m}$, assuming a linear ICP distribution and using the distance between the inner and outer surfaces of the idealized sphere to represent the distance between these pressures.

The mean PVS pressure curve was very similar to the ICP curve, as illustrated in Figure 6.3a. The PVS had a time-averaged pressure of 10.07 mmHg and a peak pulse pressure amplitude of 3.22 mmHg. A small spatial pressure gradient was observed in this network, characterized by the PVS pressure in the middle section of the sphere oscillating relative to the pressure on the boundaries. This oscillation is illustrated in Section 6.1 showing the spatial pressure distribution at the beginning of the cardiac cycle ($\Delta t_a = 0.0$) and during the peak in ICP ($\Delta t_a = 0.4$). The time-average pressure in the ECS had a value of 9.99 mmHg. The maximal temporal variation in mean ECS pressure was calculated to 1.69 mmHg, which is approximately half the equivalent value in the PVS. The spatial variation was significantly larger compared to the PVS, with a maximum spatial variation of 5.19 mmHg compared to an equivalent value in the PVS of 0.055 mmHg. This difference is illustrated in Figure 6.4 with the pressure distributions of the ECS (located on the right side) having a larger difference between the minimal and maximal pressure compared to the equivalent PVS pressures (located on the left side). The discrepancy between the ICP and the mean ECS pressure was also much larger, as illustrated in Figure 6.3b.

The standalone PVS configuration (see Table 3.2) that used a constant ICP on the surface boundaries had pressures with time-averaged values that were nearly equal to those of the standard PVS configuration. The pulse pressure amplitudes were significantly lower. The arteriole/capillary network had a peak temporal variance of 2.11 mmHg (compared to 5.06 mmHg for the standard model). An even higher difference between the two configurations was observed for the pulsating pressure in the PVS, with peak temporal differences of 0.042 mmHg (compared to 3.22 mmHg).
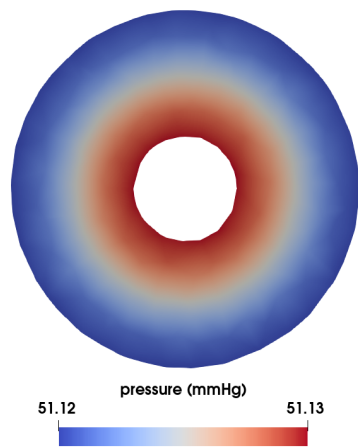
(a) Arteriole network, $\Delta t_a = 0.0$
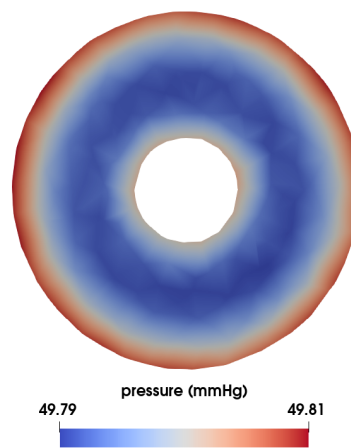
(b) Arteriole network, $\Delta t_a = 0.0$
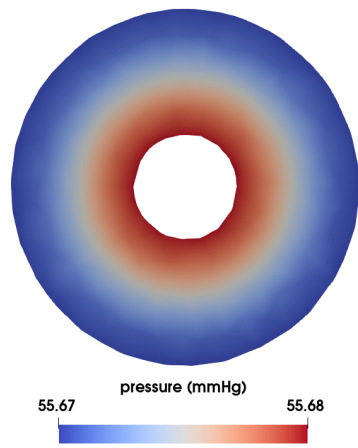
(c) Arteriole network, $\Delta t_a = 0.4$
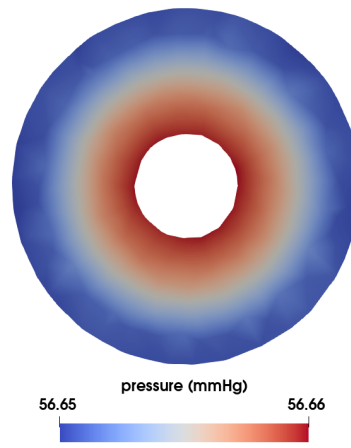
(d) Arteriole network, $\Delta t_a = 0.4$
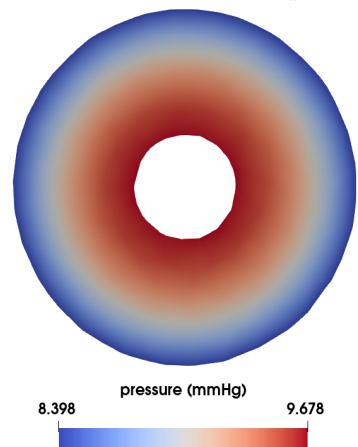
(e) Vein network, $\Delta t_a = 0.0$
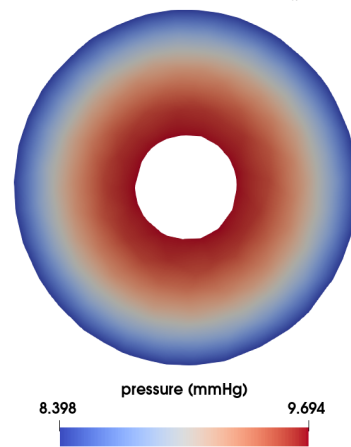
(f) Vein network, $\Delta t_a = 0.0$

Figure 6.2: Spatial pressure distribution in the blood networks. Plots of the standard PVS configuration are located on the left (a,c,e) and plots of the ECS configuration are located on the right (b,d,f). Δt_a represents the time passed after the beginning of the cardiac cycle.
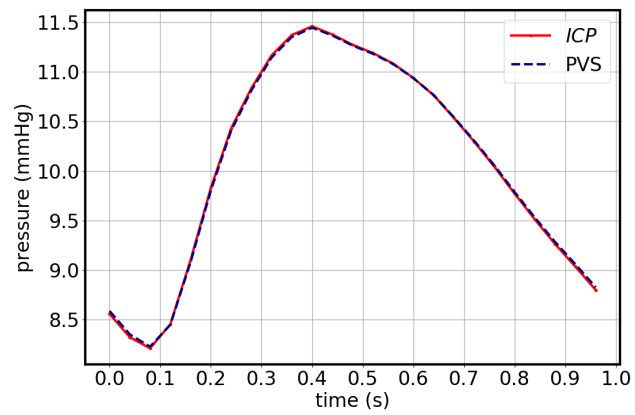
(a) Intracranial pressure for the standard PVS configuration
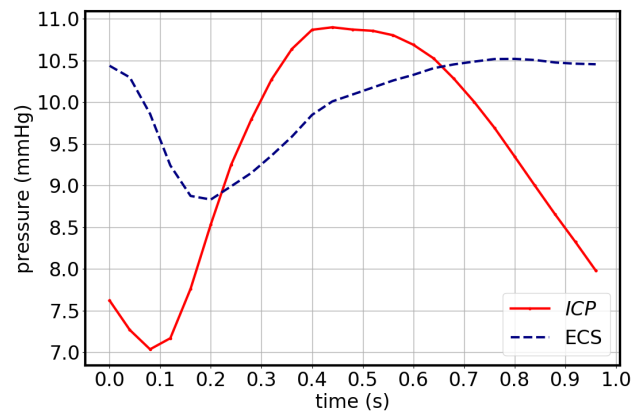
(b) Intracranial pressure for the ECS configuration
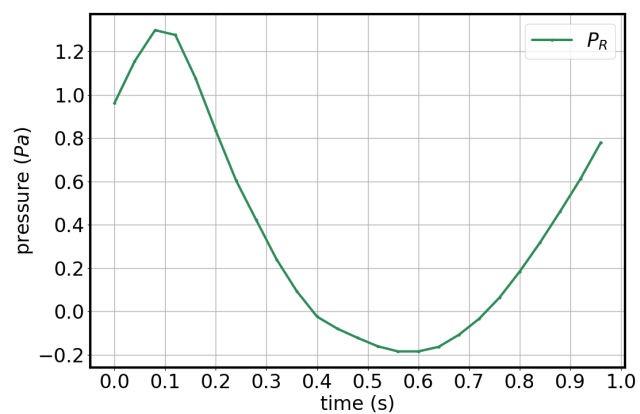
(c) Relative ventricular pressure for the standard configuration

Figure 6.3: Plot of the intracranial pressure (ICP) during a single cardiac cycle. The mean fluid network pressures (PVS/ECS) are used as a measure of ICP inside of the brain tissue. The plotted solution was extracted after 40 seconds of simulation time.

(a) PVS, $\Delta t_a = 0.0$

(b) ECS, $\Delta t_a = 0.0$

(c) PVS, $\Delta t_a = 0.4$

(d) ECS, $\Delta t_a = 0.4$
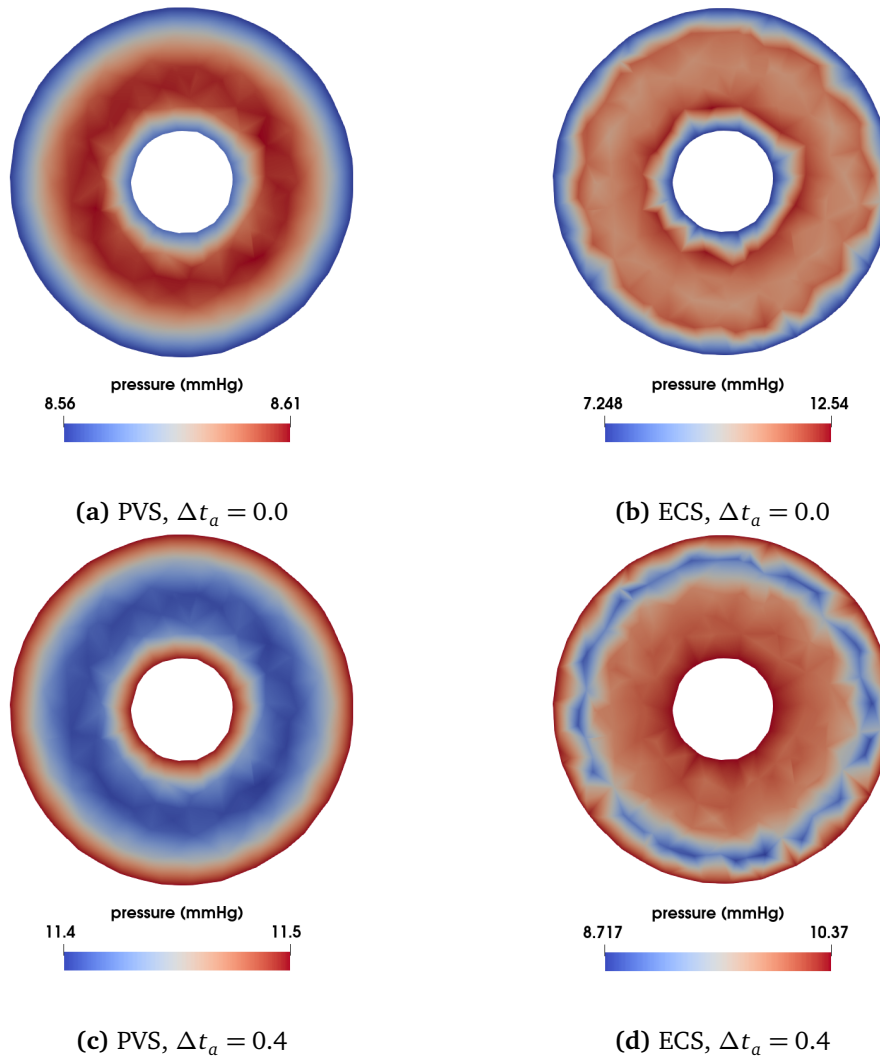
Figure 6.4: Spatial pressure distribution in the blood networks. Plots of the standard PVS configuration are located on the left (a,c,e) and plots of the ECS configuration are located on the right (b,d,f). Δt_a represents the time passed after the beginning of the cardiac cycle.

6.2 Displacements and Flow Rates

The relative volume displaced by the cortical and ventricular surfaces was calculated by Equation (4.4). A plot of the volume displaced by these surfaces is shown in Figure 6.5. The plots give a direct measure of how much volume of CSF is displaced in the SAS and ventricles during the cardiac cycle.
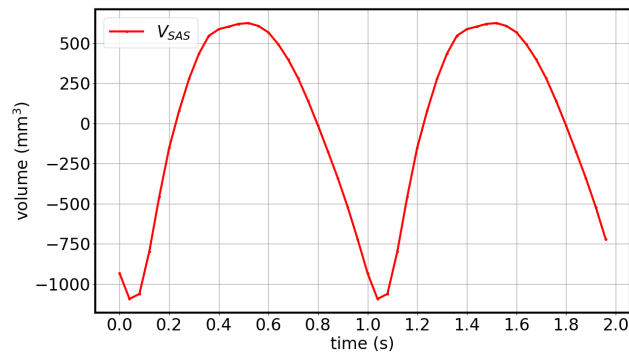
(a) Volume deformation of the cortical surface
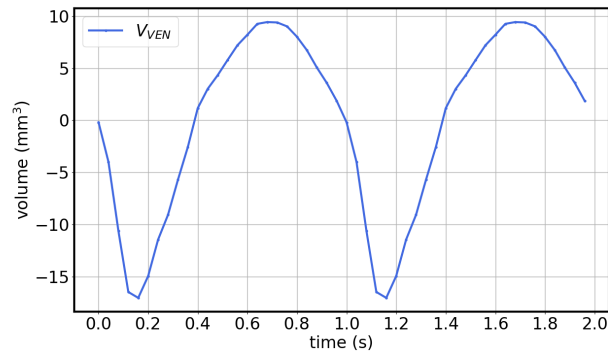
(b) Volume deformation of the ventricular surface

Figure 6.5: Plots of volume expansion for the cortical and the ventricular surfaces, extracted over two cardiac cycles.

The maximum value of tissue displacement was located on the cortical surface with a value of 0.849 mm and 0.886 mm for the standard PVS configuration and the ECS configuration, respectively. However, as explained in Chapter 4, the absolute value of tissue displacement is not representative of the relative motion of tissue during the cardiac cycle. This relative motion of the tissue is extracted by Equation (4.5) with the reference displacement field defined at $\Delta t_a = 0.04$ representing the time at which the total volume of intracranial blood is minimized. The maximum value of the relative displacement was extracted as 0.032 mm for the standard PVS configuration and 0.028 mm for the ECS configuration. In Fig-

ure 6.6, the displacement field of the standard PVS configuration is shown. The figure shows the difference between the absolute and relative displacement fields and also illustrates that the calculation of the relative displacements using Equation (4.5) is a valid measure of total tissue motion during the cardiac cycle, since all displacements point outward (at all time steps) and no change in displacement direction occurs at any time.
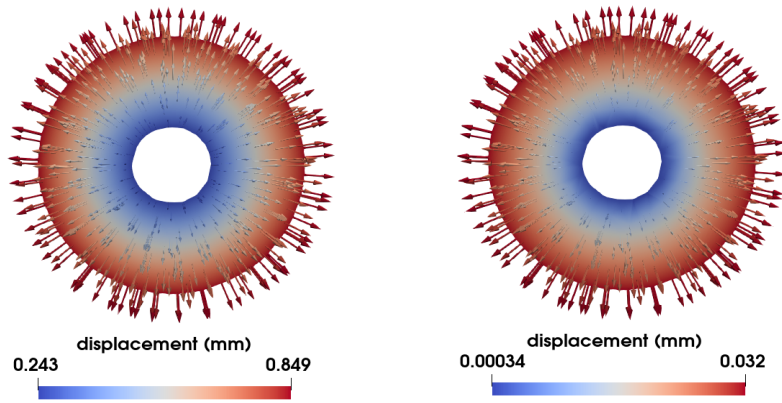
(a) Absolute displacements at $\Delta t_a = 0.44$

(b) Relative displacements at $\Delta t_a = 0.44$

Figure 6.6: Comparison between the absolute displacement field and the relative displacement field for the standard PVS configuration at $\Delta t_a = 0.44$. The domain was radially expanded outwards at all times and minimized at $\Delta t_a = 0.04$ which illustrate that the relative displacement field in Equation (4.5) can be used as a direct measure of tissue motion during the cardiac cycle.

The average bulk flow velocities of each network are calculated by Equation (4.2). This velocity denotes the Darcy velocity averaged in space and will be mostly referred to as the bulk flow velocity. This velocity is not to be confused with the time-average bulk flow velocity, which is the Darcy velocity averaged in both time and space. The arteriole network of the standard PVS configuration had a time-averaged bulk flow velocity of $0.94\frac{\mu m}{s}$ and peak bulk flow velocities of $1.51\frac{\mu m}{s}$. A small pressure gradient was observed from the ventricles and outward toward the SAS in the arteriole network, illustrated in Figures 6.2a and 6.2c. This gradient induces a small flow that points radially outward at all time steps. Velocities in the arteriole network were significantly higher for the ECS configuration due to the larger spatial variation in pressure, illustrated in Figures 6.2b and 6.2d. For this configuration, the time-average bulk velocity was calculated to be $4.78\frac{\mu m}{s}$ and with peak values as high as $14.5\frac{\mu m}{s}$. The vein network had a time-average bulk flow velocity of $0.17\frac{mm}{s}$ for both the standard PVS configuration and the ECS configuration. The difference between the velocity of the time-average bulk flow and the peak bulk flow was negligible for all configurations.

A time-average bulk flow velocity of $21.7\frac{\mu m}{s}$ was obtained in the PVS, with peaks of $40.0\frac{\mu m}{s}$. The fluid velocity in this network followed a pattern of net CSF inflow during the rise in arterial blood volume, and net outflow as the blood volume decreased. This flow pattern is illustrated in Figures 6.7a and 6.7b showing the total exchange of CSF on the cortical and ventricular surfaces, respectively. Using the ECS configuration for the third fluid network resulted in a time-average bulk flow velocity of $0.19\frac{\mu m}{s}$ and peak values of $0.46\frac{\mu m}{s}$. Compared to the difference in permeability between PVS and ECS of four orders of magnitude, a larger difference between average bulk flows could be expected. The ECS velocity is comparatively higher because of the relatively large spatial variation in the domain. This large variation (compared to the PVS) is caused by the low permeability of the network and the added boundary resistance, which delays the equalization of the fluid network pressure with the ICP. In comparison, the high permeability of the PVS causes a rapid equalization between the mean network pressure and the ICP at the boundary, leading to smaller pressure gradients, as illustrated in Figure 6.4.

Figure 6.7c illustrates the total flow rate of CSF through the cerebral aqueduct. The flow rate through the modeled cerebral aqueduct had a peak (minimum) value of -0.053 mL/s and a net flow rate of -0.015 mL/s with a negative sign denoting the directionality of the flow from the ventricles to the SAS. This net flow is induced by an elevated relative ventricular pressure as seen in Figure 6.3c, which is again caused by a net CSF efflux of 0.015 mL/s across the ventricular surface, and a net influx of 0.015 mL/s across the cortical surface to balance the additional CSF volume. This results in a circulatory effect of net CSF flow through the parenchyma, into the ventricles, and out through the cerebral aqueduct.
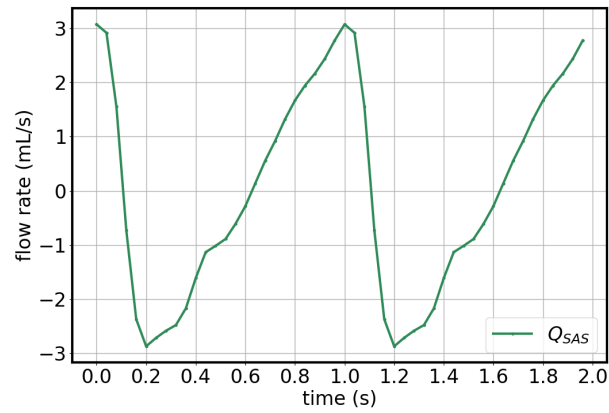
(a) Total CSF exchange over the cortical surface
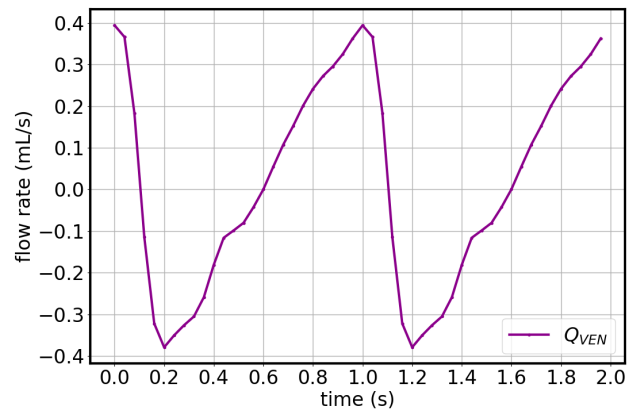
(b) Total CSF exchange over the ventricular surface
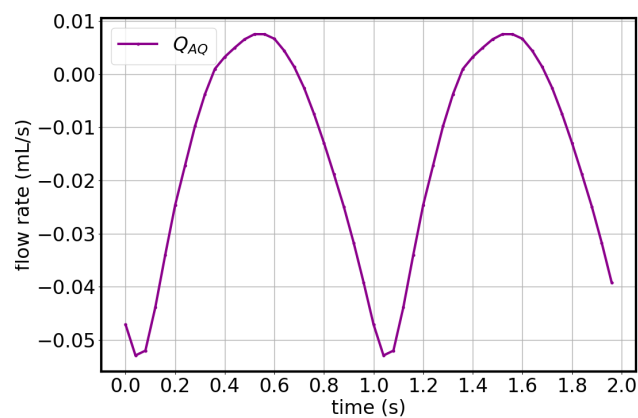
(c) Flow rate through the cerebral aqueduct

Figure 6.7: Plots of CSF flow rates over the cortical and the ventricular surfaces, as well as flow rate through the cerebral aqueduct. The plots are extracted from the standard PVS configuration and plotted over two cardiac cycles.

Table 6.1: Flow rates and flow discrepancies between the different fluid networks.

N	Q_{12}	Q_{13}	Q_{32}	ΔQ_1	ΔQ_2	ΔQ_3
13	11904.4	1161.1	1232.83	0.1	-954.53	71.7
15	11904.1	1161.32	1221.67	0.02	-804.57	60.35
17	11904.1	1161.36	1220.12	0.06	-708.22	58.8
20	11904.2	1161.61	1209.95	0.41	-613.55	48.34

6.3 Sensitivity Study on Transfer Rates

A summary of the mesh sensitivity study can be found in Table 6.1. The various mesh refinements are defined by N which indicates the number of divisions along the diameter of the sphere. All reported values are mean values over four cardiac cycles, which corresponds to four seconds of simulation time. The average transfer rate from network "i" into network "j" was calculated as

$$Q_{ij} = \frac{1}{\Delta t} \int_t^{t+\Delta t} \int_\Omega \eta_{j \leftarrow i}(p_i - p_j) d\Omega dt$$

with $\Delta t = 4$ s. In addition, the discrepancies between the flow rates are defined, with a positive sign quantifying a non-physical accumulation of fluid in each network. These discrepancies were calculated as

$$\Delta Q_i = Q_{i,\text{out}} - Q_{i,\text{in}}$$

where $Q_{i,\text{out}}$ and $Q_{i,\text{in}}$ include all contributions from the different flows entering and exiting each network i. In addition to the flows exchanging fluid between networks, these contributions also include the average arterial flow into the arteriole network and the average venous flow out of the vein network. For the PVS network, it was assumed that a zero-average exchange of CSF would occur after a stable periodic ICP.

All of the sphere meshes had some small accumulation of fluid in the arteriole network, but compared to the other networks, these values were negligible. The largest accumulation was reported for the finest mesh ($N = 20$) with a value of $\Delta_1 = 0.41$ (mm^3/s). The accumulation of fluid in the PVS was significantly larger than in the arteriole network for all meshes. The largest value was found for the coarsest mesh ($N = 13$), with a decreasing discrepancy for the finer meshes.

For the vein network, large discrepancies were observed for all meshes, with the negative sign denoting loss of fluid. The largest discrepancy was observed for the coarsest mesh, with a significant decrease for each finer mesh.

Chapter 7

Discussion

7.1 Summary

This thesis has demonstrated that combining an MPET model for the brain and a compartment model for the surrounding CSF enables a coupled model that can replicate the dynamic interplay of intracranial pulsatility. The combined model included three fluid networks for the brain and two pressures for the CSF compartments, resulting in a distribution of displacements and pressures that are in good agreement with clinical measurements. Not only in terms of replicating average values over time, but also in terms of replicating temporal variations following cardiac pulsations. The thesis also shows that coupling of the models using a combination of surface expansion, CSF exchange, and traction-based boundary conditions is a promising strategy for replicating intracranial pulsatility.

7.2 Discussion on Pulsatility

7.2.1 Pressure Variations

In general, the pulse pressure amplitudes and the time-averaged pressures agree well with clinical measurement for all three fluid networks, as well as for the ICP. The mean pressure of the arteriole/capillary blood network was almost perfectly correlated with the target mean pressure of 50 mmHg. This illustrates the effectiveness of estimating the transfer coefficients based on a target pressure drop and mass conservation, as discussed in Chapter 4. The resulting pulse pressure in the arteriole/capillary network was in the lower range of values, indicating characteristics equivalent to those of capillary blood vessels[70]. The vein pressure also replicated the desired behavior, with small temporal variations and mean pressure values within the target range. The slight increase in venous pressure during the diastolic phase (see Figure 6.1b) is expected and facilitates an increased venous outflow, as explained by Baledént [1].

The mean PVS pressure and the ICP were almost equal in size and shape, supporting the observations of Wagshul, Eide, and Madsen[2] who reported that ICP measurements are similar regardless of location. This applies not only to measurements in the ventricles versus SAS, but also to measurements in brain tissue. However, the ECS configuration had significant spatial variability in ECS pressure instead of the expected uniform distribution observed for the simulated PVS. Using a higher permeability would decrease this variation but would also lead to large velocities, which will be discussed in the next section. The pulse amplitude of the simulated ICP is in the lower specter of clinically observed values, but still within a realistic physiological range. The obtained amplitude (3.2 mmHg) compares closer to measurements found in patients with idiopathic normal pressure hydrocephalus (iNPH). Eide [66] measured temporal ICP amplitudes between $1.5 - 6.8$ mmHg for iNPH patients. Similarly, Vinje et al.[11] used measurements from iNPH patients with typical ICP amplitudes of $4 - 5$ mmHg. An explanation for why this amplitude is smaller than expected could be contributed to a smaller surface area of the idealized geometry compared to the cortical surface, which is a highly folded sheet with most of its surface area buried within these folds[99]. The decrease in surface area will lead to lower values for the overall expansion of brain volume, leading to smaller variations in ICP.

Several studies have reported multiple peaks in the ICP[2, 100] usually restricted to three peaks. Regarding the morphology of the ICP-curve, the larger characteristics of the simulated ICP are similar to the general shapes of measured curves (see, for instance Eide[66]), however these reported peaks in ICP are not replicated by the current model. Causemann et al. [27] replicated similar peaks after lowering the spinal compliance of their model from its original configuration, which could indicate that a spinal compartment pressure should be included to facilitate additional peaks. Carrera et al. [101] found that the first peak was related to the peak of arterial influx, while the second and third were associated with peak values of cerebral blood volume. The uniform source term applied in this thesis implies that the peak in arterial influx and the peak in cerebral blood volume occur simultaneously. Instead, imposing arterial inflow as a velocity on the boundary might induce several modes of deformation, leading to subsequent peaks in ICP.

The small temporal variation of the PVS pressure observed when a constant ICP was applied to the domain boundaries implies that an MPET model with linear transfer terms cannot propagate its pulsatile variation from the arteries down to PVS/ECS networks to describe a realistic variation of ICP. Some additional component is needed to account for the rigid confinement of the skull, which the nonlinear ICP does for the combined model proposed here. Eliussen et al. [72] included an example of a pulsatile MPET model with ICP on the boundaries described by a compartment model with constant compliance. This resulted in a very small temporal variability of pressure in the PVS, which further indicates this finding.

7.2.2 Displacements

Peak displacements are in the lower range of values compared to clinical measurement, but still within a physical range. Greitz et al.[71] Poncelet et al.[38] and Enzmann and Pelc[39] all used MRI techniques to measure the motion of brain tissue. These studies reported peak displacements in the range of $0.1 - 0.5$ mm. In more recent work based on similar MRI techniques, Pahlavian et al.[40] found peak displacements of 0.187 ± 0.05 mm located on the brain stem. Sloots et al.[102] also found that the peak displacements are located on the brain stem, with values of approximately 0.2 mm. The symmetric pattern of displacements observed for the idealized geometry of this study is not very comparable to the asymmetric displacement fields observed in the brain and especially not in thin elongated structures such as the brain stem. Pahlavian et al.[40] also reported peak displacements in other regions of the brain such as the corpus callosum ($65 \pm 15 \mu m$), the cingulate gyrus ($43 \pm 10 \mu m$) and the parietal lobe ($31 \pm 4 \mu m$). These regions are located above the ventricles and are more comparable to the spherical geometry of the model in this thesis, for which the peak displacements of $38 \mu m$ agree well.

7.2.3 Flow rates

Estimates of fluid network velocities which are related to the bulk flow velocities by $v = \frac{q}{\phi}$ resulted in mean PVS velocities in the range of $5.37 \frac{mm}{s}$ to $14.1 \frac{mm}{s}$ using PVS porosities between $1.54 \cdot 10^{-3}$ and $4.04 \cdot 10^{-3}$. These porosities were estimated based on measurements of total PVS volumes (see Section 4.1 for further details). The estimated mean PVS velocities are significantly higher than most estimates from experimental studies. Mestre et al. [12] measured typical net flow velocities of $18.7 \frac{\mu m}{s}$ with peak temporal variations of approximately $20 \frac{\mu m}{s}$. Bedussi et al. [13] obtained similar results for the net velocities with values of $17 \frac{\mu m}{s}$. The peak variation in PVS velocities found in Bedussi et al. [13] was significantly higher compared to Mestre et al. [12], with values in the range of $100 - 200 \frac{\mu m}{s}$, when the rapid cardiac cycles are taken into account[24]. The ECS had fluid velocities in the range of $0.83 \frac{\mu m}{s}$ to $1.37 \frac{\mu m}{s}$. However, since only estimates of the bulk flow for the ECS exist in literature, the time-average bulk velocity of $0.19 \frac{\mu m}{s}$ is more relevant to compare. According to some studies [103] [104] the estimated velocities of the bulk ISF flow are in the range of $0.1 - 0.24 \frac{\mu m}{s}$, which agree well with the modeled result.

The model in this study illustrates the possibility of representing flow through the cerebral aqueduct using a relative ventricular pressure. The peak amplitude and the aqueductal stroke volume correlate fairly well with the clinical indicators defined in Table 4.1, although the net flow of $0.015 \frac{mL}{s}$ from the ventricles to the SAS is large compared to some studies that estimate CSF production rates in the ventricles in the order of $10^{-3} \frac{mL}{s}$[45, 105, 106]. Note that the timing of the peak aqueductal flow is poorly correlated with the observed pattern measured by Baledént [1] (illustrated in Figure 2.5). This may indicate that constant compli-

ance does not facilitate the exponential pressure-volume relation observed within the cranium[49], or that the simplified geometry of the ventricles causes an unrealistic pattern of displacements of the ventricular wall. However, since the relative ventricular pressure is negligible compared to the size in the temporal variations of the ICP, the effect of this pressure is likely not very influential to the overall behavior of the model.

Figure 6.7a shows that CSF is pushed into the brain over the cortical surface during the increase in arterial blood volume and ICP. The timing of the peak CSF influx supports the idea that heart rate functions as a "periarterial pump"[14, 15]. However, the model used in this thesis can recreate the macroscale characteristics of CSF influx during systole without directly modeling arterial vasodilation. In the current model, the oscillatory movement of CSF over the cortical surface is driven by the difference between the ICP on the boundary and the inner pressure that oscillates relative to the boundary, as illustrated in Section 6.1. A small net flow of CSF over the cortical surface and through perivascular spaces is caused by the additional volume of CSF that flows out of the cerebral aqueduct, which subsequently increases ICP in the SAS relative to the brain and induces a net influx over the cortical surface. This indirectly supports the findings of Kedarasetti et al. [25], in which they did not find direct support for the "periarterial pump" mechanism driving net CSF influx by motion of arterial walls alone. However, Kedarasetti et al. found support for net flow of CSF through PVS driven by functional hyperemia in several studies[25, 26], which is not taken into account in the model of this thesis. Similarly, Daversin-Catty et al. [24] suggested that pulsatile PVS flow is accompanied by a small pressure gradient of uncertain origin, as their model did not replicate a net flow through PVS by only including arterial wall motion. When a static pressure gradient of $1.5 \frac{\text{mmHg}}{m}$ was included in their model, they obtained a net flow of $20 \frac{\mu m}{s}$ to $30 \frac{\mu m}{s}$ through the PVS[24]. Although the added volume of aqueductal outflow in the model in this thesis facilitates a net influx of CSF over the cortical surface, its small size is likely not large enough to explain the influx of CSF observed in several clinical studies by tracking tracers in CSF[12, 13], and similarly to the conclusions made by Daversin-Catty et al. [24], some additional static or pulsatile gradient would be needed to explain such an influx.

7.3   Numerical Accuracy

The mesh sensitivity study demonstrated that the finer meshes conserved the total fluid volume better than the coarser meshes. The arteriole network had a much smaller discrepancy in fluid conservation compared to the PVS and vein network. In these networks, the discrepancies were much larger and increased with the coarseness of the mesh. The reason why the arteriole network conserved fluid volume much better than in the PVS and vein network is because of the different flow rates on the boundaries of the fluid networks. Józsa et al. [97] explained how fluid transfer between networks mitigates small errors compared to fluid transfer

across boundaries. They showed that these errors can be significant when first-order polynomials are used for the fluid network pressure, and that using a combination of higher-order polynomials and local mesh refinement on the boundary can drastically reduce these errors. Similar discoveries were made in this thesis; since the arteriole network imposes a zero flux boundary condition, the error generated from the surface flow will be much smaller compared to the errors generated in the other fluid networks, where comparatively large rates of fluid crosses the boundaries.

Most earlier MPET studies on the brain have prescribed the influx and efflux of blood directly to the boundary of the cortical surface using Dirichlet or Neumann conditions[28–33]. Some exceptions include Eliussen et al. [72] and Causemann et al. [27] (technically not an MPET study due to only one modeled network), who both used a uniform pulsatile source term to induce pulsatility. Prescription of such flow over boundary surfaces may not ensure fluid conservation in the system. Modeling arterial blood flow into the brain through a source term is likely to be better with respect to numerical accuracy, as demonstrated for the arteriole network in this thesis. However, inaccurate arterial inflow only implies that the blood volume entering the brain will not necessarily match the prescribed amount. Therefore, only the input of the model will be affected and not the actual accuracy of the model. Similarly for this thesis, only the output of the inaccurate measurement of venous outflow is affected, and not the accuracy of the model itself. However, the exchange of CSF across the domain surfaces will affect the model, since it directly influences the ICP. Therefore, any inaccuracy in calculating this exchange rate will affect the overall accuracy of the simulation.

7.4 Limitations

Geometry The fact that an idealized geometry was used for the simulations is one of the main limitations of this study. As the study aimed to quantitatively replicate clinical measurements, the use of a realistic geometry could have had a significant impact on the results. It is noted that the original goal of the thesis was to use a patient-specific brain geometry but was found to be difficult due to instabilities.

Uncertain parameter estimations Several material parameters were estimated in the current model and not all of these estimates were considered on the basis of mathematical principles and material properties. The Biot-Willis coefficients (α_j) and the storage coefficients (S_j) were crudely estimated based on a combination of extensive testing and the expected compliance of the respective fluid networks. Transfer coefficients were effectively estimated using principles of mass conservation. However, the distribution of fluid flow between networks is highly uncertain, which could result in poor estimates for these coefficients.

Instabilities   Numerical instabilities have been present for various geometries and model parameters throughout the work of this thesis. These instabilities were mainly an artifact of the singular system caused by the pure traction boundary conditions, as well as the large temporal gradients induced by low values for the storage coefficients. In this study, no theoretical analysis of the stability and convergence of solutions was performed. Gaining a better understanding of these instabilities could perhaps lead to greater flexibility in modeling decisions.

Relative ventricular pressure   Flow through the cerebral aqueduct is governed by the relative ventricular pressure, which uses a constant compliance that does not account for the larger variations in ICP. The relative ventricular pressure could have an exponential pressure-volume relationship, indicated by clinical measures of craniospinal compliance. The fact that the modeled aqueductal flow poorly replicated the morphology of measurements of this flow is an indication that the model needs more work.

Spinal compliance   The damping effect of the high-compliant spinal sac was not included in the current model. Instead, the effect of displaced CSF in the SAS was lumped into a single compartment model for ICP. Its effect could be modeled by including an additional pressure to the compartment model.

7.5   Conclusions

The model presented in this thesis illustrates that it is possible to reproduce large temporal variations in cardiac-induced pulsatility using MPET modeling. However, more work is needed to obtain a model that can replicate instantaneous changes in ICP in brain tissue, as well as maintain fluid network velocities within a realistic range.

An important aspect of modeling pulsatility in MPET-type models was discovered. Compared to a simplified version that only included linear components, the proposed model illustrated that pressure pulsations generated by direct fluid transfer to perivascular spaces are not large enough to replicate intracranial pulsatility alone. The simplified (standalone) model resulted in pressure variations in PVS that are significantly lower than clinically measured values suggest[2]. Using larger values for the transfer coefficients would likely increase PVS pulsatility but would likely lead to unrealistic values for the transfer rates between the arterioles and the PVS.

The resulting model also illustrates the effectiveness of targeting specific pressures by adjusting various model parameters. The mean ICP can be effectively adjusted by the baseline pressure P_0. The pressures of the blood networks can

also be effectively adjusted based on estimating the transfer coefficients. Generating sufficiently large pressure amplitudes can be facilitated by a low storage coefficient, although this may lead to instabilities.

This thesis introduced a relative ventricular pressure, which represents the spatial variance of ICP. The pressure facilitated a realistic amplitude for the aqueductal flow rate, but more work is needed to obtain a realistic morphology of its flow curve. Although this pressure has small effects on the overall behavior of the model, studying it further could lead to a better understanding of the transmantle pressure gradient and how and if it affects CSF clearance through the brain.

Future work includes verifying the model on patient-specific geometries, and assess the influence of asymmetric deformation patterns caused by a realistic brain geometry. To facilitate this, more work on stability measures for MPET models with pure traction boundary conditions and large temporal variation is likely required. In addition, extending the proposed model with additional fluid networks such as an arterial network and separate networks for the PVS and ECS, as well as extending the compartment model with a pressure for spinal CSF is likely an important step to further improve the clinical realism of this model.

Bibliography

[1] O. Balédent, "Imaging of the cerebrospinal fluid circulation," in *Adult Hydrocephalus*, D. Rigamonti, Ed. Cambridge University Press, 2014, pp. 121–138. DOI: `10.1017/CB09781139382816.013`.

[2] M. Wagshul, P. Eide, and J. Madsen, "The pulsating brain: A review of experimental and clinical studies of intracranial pulsatility," English (US), *Fluids and Barriers of the CNS*, vol. 8, no. 1, Jan. 2011, Funding Information: MEW acknowledges the support of the Brain Child Foundation, and JRM acknowledges the support in part by a gift from the Webster family., ISSN: 2045-8118. DOI: `10.1186/2045-8118-8-5`.

[3] J. J. Schubert, M. Veronese, L. Marchitelli, B. Bodini, M. Tonietto, B. Stankoff, D. J. Brooks, A. Bertoldo, P. Edison, and F. E. Turkheimer, "Dynamic 11c-pib pet shows cerebrospinal fluid flow alterations in alzheimer disease and multiple sclerosis," *Journal of Nuclear Medicine*, vol. 60, no. 10, pp. 1452–1460, Mar. 2019. DOI: `10.2967/jnumed.118.223834`. [Online]. Available: `https://doi.org/10.2967/jnumed.118.223834`.

[4] E. K. Lindstrøm, G. Ringstad, K.-A. Mardal, and P. K. Eide, "Cerebrospinal fluid volumetric net flow rate and direction in idiopathic normal pressure hydrocephalus," *NeuroImage: Clinical*, vol. 20, pp. 731–741, 2018. DOI: `10.1016/j.nicl.2018.09.006`. [Online]. Available: `https://doi.org/10.1016/j.nicl.2018.09.006`.

[5] G. Ringstad, E. K. Lindstrøm, S. A. S. Vatnehol, K.-A. Mardal, K. E. Emblem, and P. K. Eide, "Non-invasive assessment of pulsatile intracranial pressure with phase-contrast magnetic resonance imaging," *PLOS ONE*, vol. 12, no. 11, L. M. Cavallo, Ed., e0188896, Nov. 2017. DOI: `10.1371/journal.pone.0188896`. [Online]. Available: `https://doi.org/10.1371/journal.pone.0188896`.

[6] P. K. Eide, M. Czosnyka, W. Sorteberg, J. D. Pickard, and P. Smielewski, "Association between intracranial, arterial pulse pressure amplitudes and cerebral autoregulation in head injury patients," *Neurological Research*, vol. 29, no. 6, pp. 578–582, Sep. 2007. DOI: `10.1179/016164107x172167`. [Online]. Available: `https://doi.org/10.1179/016164107x172167`.

[7] P. K. Eide and A. Brean, "Intracranial pulse pressure amplitude levels determined during preoperative assessment of subjects with possible idiopathic normal pressure hydrocephalus," *Acta Neurochirurgica*, vol. 148, no. 11, pp. 1151–1156, Oct. 2006. DOI: 10.1007/s00701-006-0896-0. [Online]. Available: https://doi.org/10.1007/s00701-006-0896-0.

[8] W. M. Pardridge, "Drug transport in brain via the cerebrospinal fluid," *Fluids and Barriers of the CNS*, vol. 8, no. 1, Jan. 2011. DOI: 10.1186/2045-8118-8-7. [Online]. Available: https://doi.org/10.1186/2045-8118-8-7.

[9] T. P. Santisakultarm, N. R. Cornelius, N. Nishimura, A. I. Schafer, R. T. Silver, P. C. Doerschuk, W. L. Olbricht, and C. B. Schaffer, "In vivo two-photon excited fluorescence microscopy reveals cardiac- and respiration-dependent pulsatile blood flow in cortical blood vessels in mice," *American Journal of Physiology-Heart and Circulatory Physiology*, vol. 302, no. 7, H1367–H1377, Apr. 2012. DOI: 10.1152/ajpheart.00417.2011. [Online]. Available: https://doi.org/10.1152/ajpheart.00417.2011.

[10] N. E. Fultz, G. Bonmassar, K. Setsompop, R. A. Stickgold, B. R. Rosen, J. R. Polimeni, and L. D. Lewis, "Coupled electrophysiological, hemodynamic, and cerebrospinal fluid oscillations in human sleep," *Science*, vol. 366, no. 6465, pp. 628–631, Nov. 2019. DOI: 10.1126/science.aax5440. [Online]. Available: https://doi.org/10.1126/science.aax5440.

[11] V. Vinje, G. Ringstad, E. K. Lindstrøm, L. M. Valnes, M. E. Rognes, P. K. Eide, and K.-A. Mardal, "Respiratory influence on cerebrospinal fluid flow–a computational study based on long-term intracranial pressure measurements," *Scientific reports*, vol. 9, no. 1, pp. 1–13, 2019.

[12] H. Mestre, J. Tithof, T. Du, W. Song, W. Peng, A. M. Sweeney, G. Olveda, J. H. Thomas, M. Nedergaard, and D. H. Kelley, "Flow of cerebrospinal fluid is driven by arterial pulsations and is reduced in hypertension," *Nature Communications*, vol. 9, no. 1, Nov. 2018. DOI: 10.1038/s41467-018-07318-3. [Online]. Available: https://doi.org/10.1038/s41467-018-07318-3.

[13] B. Bedussi, M. Almasian, J. de Vos, E. VanBavel, and E. Bakker, "Paravascular spaces at the brain surface: Low resistance pathways for cerebrospinal fluid flow," *Journal of Cerebral Blood Flow & Metabolism*, vol. 38, Oct. 2017. DOI: 10.1177/0271678x17737984.

[14] P. Hadaczek, Y. Yamashita, H. Mirek, L. Tamas, M. Bohn, C. Noble, J. Park, and K. Bankiewicz, "The "perivascular pump" driven by arterial pulsation is a powerful mechanism for the distribution of therapeutic molecules within the brain," *Molecular therapy : the journal of the American Society of Gene Therapy*, vol. 14, pp. 69–78, Aug. 2006. DOI: 10.1016/j.ymthe.2006.02.018.

[15] P. Wang and W. Olbricht, "Fluid mechanics in the perivascular space," *Journal of theoretical biology*, vol. 274, pp. 52–7, Apr. 2011. DOI: `10.1016/j.jtbi.2011.01.014`.

[16] A. A. Linninger, K. Tangen, C.-Y. Hsu, and D. Frim, "Cerebrospinal fluid mechanics and its coupling to cerebrovascular dynamics," *Annual Review of Fluid Mechanics*, vol. 48, no. 1, pp. 219–257, Jan. 2016. DOI: `10.1146/annurev-fluid-122414-034321`. [Online]. Available: `https://doi.org/10.1146/annurev-fluid-122414-034321`.

[17] J. J. Iliff, M. Wang, Y. Liao, B. A. Plogg, W. Peng, G. A. Gundersen, H. Benveniste, G. E. Vates, R. Deane, S. A. Goldman, E. A. Nagelhus, and M. Nedergaard, "A paravascular pathway facilitates CSF flow through the brain parenchyma and the clearance of interstitial solutes, including amyloid β," *Science Translational Medicine*, vol. 4, no. 147, Aug. 2012. DOI: `10.1126/scitranslmed.3003748`. [Online]. Available: `https://doi.org/10.1126/scitranslmed.3003748`.

[18] M. Rennels, O. Blaumanis, and P. Grady, "Rapid solute transport throughout the brain via paravascular fluid pathways.," *Advances in neurology*, vol. 52, pp. 431–439, 1990.

[19] P. Hadaczek, Y. Yamashita, H. Mirek, L. Tamas, M. C. Bohn, C. Noble, J. W. Park, and K. Bankiewicz, "The "perivascular pump" driven by arterial pulsation is a powerful mechanism for the distribution of therapeutic molecules within the brain," *Molecular Therapy*, vol. 14, no. 1, pp. 69–78, 2006.

[20] J. J. Iliff, M. Wang, D. M. Zeppenfeld, A. Venkataraman, B. A. Plog, Y. Liao, R. Deane, and M. Nedergaard, "Cerebral arterial pulsation drives paravascular csf–interstitial fluid exchange in the murine brain," *Journal of Neuroscience*, vol. 33, no. 46, pp. 18 190–18 199, 2013.

[21] N. A. Jessen, A. S. F. Munk, I. Lundgaard, and M. Nedergaard, "The glymphatic system: A beginner's guide," *Neurochemical research*, vol. 40, no. 12, pp. 2583–2599, 2015.

[22] R. Carare, M. Bernardes-Silva, T. Newman, A. Page, J. Nicoll, V. Perry, and R. Weller, "Solutes, but not cells, drain from the brain parenchyma along basement membranes of capillaries and arteries: Significance for cerebral amyloid angiopathy and neuroimmunology," *Neuropathology and applied neurobiology*, vol. 34, no. 2, pp. 131–144, 2008.

[23] V. Vinje, E. N. T. P. Bakker, and M. E. Rognes, "Brain solute transport is more rapid in periarterial than perivenous spaces," *Scientific Reports*, vol. 11, no. 1, p. 16 085, Aug. 2021, ISSN: 2045-2322. DOI: `10.1038/s41598-021-95306-x`. [Online]. Available: `https://doi.org/10.1038/s41598-021-95306-x`.

[24] C. Daversin-Catty, V. Vinje, K.-A. Mardal, and M. E. Rognes, "The mechanisms behind perivascular fluid flow," *PLOS ONE*, vol. 15, no. 12, F.-B. Tian, Ed., e0244442, Dec. 2020. DOI: `10.1371/journal.pone.0244442`. [Online]. Available: `https://doi.org/10.1371/journal.pone.0244442`.

[25] R. T. Kedarasetti, P. J. Drew, and F. Costanzo, "Arterial pulsations drive oscillatory flow of CSF but not directional pumping," *Scientific Reports*, vol. 10, no. 1, Jun. 2020. DOI: `10.1038/s41598-020-66887-w`. [Online]. Available: `https://doi.org/10.1038/s41598-020-66887-w`.

[26] R. T. Kedarasetti, P. J. Drew, and F. Costanzo, "Arterial vasodilation drives convective fluid flow in the brain: A poroelastic model," *bioRxiv*, 2021. DOI: `10.1101/2021.09.23.461603`. eprint: `https://www.biorxiv.org/content/early/2021/09/24/2021.09.23.461603.full.pdf`. [Online]. Available: `https://www.biorxiv.org/content/early/2021/09/24/2021.09.23.461603`.

[27] M. Causemann, V. Vinje, and M. E. Rognes, "Human intracranial pulsatility during the cardiac cycle: A computational modelling framework," May 2022. DOI: `10.1101/2022.05.19.492650`. [Online]. Available: `https://doi.org/10.1101/2022.05.19.492650`.

[28] J. C. Vardakis, L. Guo, T. W. Peach, T. Lassila, M. Mitolo, D. Chou, Z. A. Taylor, S. Varma, A. Venneri, A. F. Frangi, and Y. Ventikos, "Fluid–structure interaction for highly complex, statistically defined, biological media: Homogenisation and a 3d multi-compartmental poroelastic model for brain biomechanics," *Journal of Fluids and Structures*, vol. 91, p. 102 641, Nov. 2019. DOI: `10.1016/j.jfluidstructs.2019.04.008`. [Online]. Available: `https://doi.org/10.1016/j.jfluidstructs.2019.04.008`.

[29] J. C. Vardakis, D. Chou, L. Guo, and Y. Ventikos, "Exploring neurodegenerative disorders using a novel integrated model of cerebral transport: Initial results," *Proceedings of the Institution of Mechanical Engineers, Part H: Journal of Engineering in Medicine*, vol. 234, no. 11, pp. 1223–1234, 2020, PMID: 33078663. DOI: `10.1177/0954411920964630`. eprint: `https://doi.org/10.1177/0954411920964630`. [Online]. Available: `https://doi.org/10.1177/0954411920964630`.

[30] L. Guo, J. C. Vardakis, T. Lassila, M. Mitolo, N. Ravikumar, D. Chou, M. Lange, A. Sarrami-Foroushani, B. J. Tully, Z. A. Taylor, S. Varma, A. Venneri, A. F. Frangi, and Y. Ventikos, "Subject-specific multi-poroelastic model for exploring the risk factors associated with the early stages of alzheimer's disease," *Interface Focus*, vol. 8, no. 1, p. 20 170 019, Dec. 2017. DOI: `10.1098/rsfs.2017.0019`. [Online]. Available: `https://doi.org/10.1098/rsfs.2017.0019`.

[31] L. Guo, Z. Li, J. Lyu, Y. Mei, J. C. Vardakis, D. Chen, C. Han, X. Lou, and Y. Ventikos, "On the validation of a multiple-network poroelastic model using arterial spin labeling MRI data," *Frontiers in Computational Neuro-*

science, vol. 13, Sep. 2019. DOI: `10.3389/fncom.2019.00060`. [Online]. Available: `https://doi.org/10.3389/fncom.2019.00060`.

[32]   L. Guo, J. C. Vardakis, D. Chou, and Y. Ventikos, "A multiple-network poroelastic model for biological systems and application to subject-specific modelling of cerebral fluid transport," *International Journal of Engineering Science*, vol. 147, p. 103 204, 2020, ISSN: 0020-7225. DOI: `https://doi.org/10.1016/j.ijengsci.2019.103204`. [Online]. Available: `https://www.sciencedirect.com/science/article/pii/S0020722519322785`.

[33]   D. Chou, J. C. Vardakis, L. Guo, B. J. Tully, and Y. Ventikos, "A fully dynamic multi-compartmental poroelastic system: Application to aqueductal stenosis," *Journal of Biomechanics*, vol. 49, no. 11, pp. 2306–2312, Jul. 2016. DOI: `10.1016/j.jbiomech.2015.11.025`. [Online]. Available: `https://doi.org/10.1016/j.jbiomech.2015.11.025`.

[34]   B. TULLY and Y. VENTIKOS, "Cerebral water transport using multiple-network poroelastic theory: Application to normal pressure hydrocephalus," *Journal of Fluid Mechanics*, vol. 667, pp. 188–215, 2011. DOI: `10.1017/S0022112010004428`.

[35]   L. Tao and K. Rajagopal, "Unsteady diffusion of fluids through a non-linearly elastic cylindrical annulus," *International Journal of Non-Linear Mechanics*, vol. 28, no. 1, pp. 43–55, 1993, ISSN: 0020-7462. DOI: `https://doi.org/10.1016/0020-7462(93)90005-6`. [Online]. Available: `https://www.sciencedirect.com/science/article/pii/0020746293900056`.

[36]   K. Rajagopal, R. Yalamanchili, and A. Wineman, "Modeling electro-rheological materials through mixture theory," *International Journal of Engineering Science*, vol. 32, no. 3, pp. 481–500, 1994, ISSN: 0020-7225. DOI: `https://doi.org/10.1016/0020-7225(94)90136-8`. [Online]. Available: `https://www.sciencedirect.com/science/article/pii/0020722594901368`.

[37]   M. Maes, E. Vandoolaeghe, J. Degroote, C. Altamura, C. Roels, and P. Hermans, "Linear CT-scan measurements in alcohol-dependent patients with and without delirium tremens," *Alcohol*, vol. 20, no. 2, pp. 117–123, Feb. 2000. DOI: `10.1016/s0741-8329(99)00066-x`. [Online]. Available: `https://doi.org/10.1016/s0741-8329(99)00066-x`.

[38]   B. P. Poncelet, V. J. Wedeen, R. M. Weisskoff, and M. S. Cohen, "Brain parenchyma motion: Measurement with cine echo-planar MR imaging.," *Radiology*, vol. 185, no. 3, pp. 645–651, Dec. 1992. DOI: `10.1148/radiology.185.3.1438740`. [Online]. Available: `https://doi.org/10.1148/radiology.185.3.1438740`.

[39]   D. R. Enzmann and N. J. Pelc, "Brain motion: Measurement with phase-contrast MR imaging.," *Radiology*, vol. 185, no. 3, pp. 653–660, Dec. 1992. DOI: `10.1148/radiology.185.3.1438741`. [Online]. Available: `https://doi.org/10.1148/radiology.185.3.1438741`.

[40] S. H. Pahlavian, J. Oshinski, X. Zhong, F. Loth, and R. Amini, "Regional Quantification of Brain Tissue Strain Using Displacement-Encoding With Stimulated Echoes Magnetic Resonance Imaging," *Journal of Biomechanical Engineering*, vol. 140, no. 8, Jun. 2018, 081010, ISSN: 0148-0731. DOI: `10.1115/1.4040227`. eprint: `https://asmedigitalcollection.asme.org/biomechanical/article-pdf/140/8/081010/5990462/bio\_140\_08\_081010.pdf`. [Online]. Available: `https://doi.org/10.1115/1.4040227`.

[41] "Primer on cerebrovascular diseases (second edition)," in *Primer on Cerebrovascular Diseases (Second Edition)*, L. R. Caplan, J. Biller, M. C. Leary, E. H. Lo, A. J. Thomas, M. Yenari, and J. H. Zhang, Eds., Second Edition, San Diego: Academic Press, 2017, ISBN: 978-0-12-803058-5. [Online]. Available: `https://www.elsevier.com/books/primer-on-cerebrovascular-diseases/caplan/978-0-12-803058-5`.

[42] W. F. Boron and E. L. Boulpaep, *Medical Physiology*, 3rd ed. Philadelphia, PA: Elsevier - Health Sciences Division, May 2016.

[43] S. Budday, R. Nay, R. de Rooij, P. Steinmann, T. Wyrobek, T. C. Ovaert, and E. Kuhl, "Mechanical properties of gray and white matter brain tissue by indentation," *Journal of the Mechanical Behavior of Biomedical Materials*, vol. 46, pp. 318–330, 2015, ISSN: 1751-6161. DOI: `https://doi.org/10.1016/j.jmbbm.2015.02.024`. [Online]. Available: `https://www.sciencedirect.com/science/article/pii/S1751616115000673`.

[44] S. Hladky and M. Barrand, "Mechanisms of fluid movement into, through and out of the brain: Evaluation of the evidence," *Fluids and Barriers of the CNS*, Dec. 2014. DOI: `10.1186/2045-8118-11-26`.

[45] H. H. Damkier, P. D. Brown, and J. Praetorius, "Cerebrospinal fluid secretion by the choroid plexus," *Physiological Reviews*, vol. 93, no. 4, pp. 1847–1892, Oct. 2013. DOI: `10.1152/physrev.00004.2013`. [Online]. Available: `https://doi.org/10.1152/physrev.00004.2013`.

[46] J. G. Betts, K. A. Young, J. A. Wise, E. Johnson, B. Poe, D. H. Kruse, O. Korol, J. E. Johnson, M. Womble, and P. DeSaix, *Anatomy and Physiology*. OpenStax, Aug. 2013. [Online]. Available: `https://openstax.org/books/anatomy-and-physiology/pages/preface`.

[47] B. Mokri, "The monro–kellie hypothesis," *Neurology*, vol. 56, no. 12, pp. 1746–1748, 2001, ISSN: 0028-3878. DOI: `10.1212/WNL.56.12.1746`. eprint: `https://n.neurology.org/content/56/12/1746.full.pdf`. [Online]. Available: `https://n.neurology.org/content/56/12/1746`.

[48] B. Mokri, "The monro-kellie hypothesis: Applications in CSF volume depletion," *Neurology*, vol. 56, no. 12, pp. 1746–1748, Jun. 2001. DOI: `10.1212/wnl.56.12.1746`. [Online]. Available: `https://doi.org/10.1212/wnl.56.12.1746`.

[49] A. Marmarou, K. Shulman, and J. LaMorgese, "Compartmental analysis of compliance and outflow resistance of the cerebrospinal fluid system," *Journal of Neurosurgery*, vol. 43, no. 5, pp. 523–534, Nov. 1975. DOI: `10.3171/jns.1975.43.5.0523`. [Online]. Available: `https://doi.org/10.3171/jns.1975.43.5.0523`.

[50] A. Wåhlin, K. Ambarki, R. Birgander, N. Alperin, J. Malm, and A. Eklund, "Assessment of craniospinal pressure-volume indices," *American Journal of Neuroradiology*, vol. 31, no. 9, pp. 1645–1650, Jul. 2010. DOI: `10.3174/ajnr.a2166`. [Online]. Available: `https://doi.org/10.3174/ajnr.a2166`.

[51] R.-W. Tain, A. M. Bagci, B. L. Lam, E. M. Sklar, B. Ertl-Wagner, and N. Alperin, "Determination of cranio-spinal canal compliance distribution by MRI: Methodology and early application in idiopathic intracranial hypertension," *Journal of Magnetic Resonance Imaging*, vol. 34, no. 6, pp. 1397–1404, Oct. 2011. DOI: `10.1002/jmri.22799`. [Online]. Available: `https://doi.org/10.1002/jmri.22799`.

[52] E. N. T. P. Bakker, B. J. Bacskai, M. Arbel-Ornath, R. Aldea, B. Bedussi, A. W. J. Morris, R. O. Weller, and R. O. Carare, "Lymphatic clearance of the brain: Perivascular, paravascular and significance for neurodegenerative diseases," *Cellular and Molecular Neurobiology*, vol. 36, no. 2, pp. 181–194, Mar. 2016. DOI: `10.1007/s10571-015-0273-8`. [Online]. Available: `https://doi.org/10.1007/s10571-015-0273-8`.

[53] J. Iliff, A. Thrane, and M. Nedergaard, "Chapter 3 - the glymphatic system and brain interstitial fluid homeostasis," in *Primer on Cerebrovascular Diseases (Second Edition)*, L. R. Caplan, J. Biller, M. C. Leary, E. H. Lo, A. J. Thomas, M. Yenari, and J. H. Zhang, Eds., Second Edition, San Diego: Academic Press, 2017, pp. 17–25, ISBN: 978-0-12-803058-5. DOI: `https://doi.org/10.1016/B978-0-12-803058-5.00003-5`. [Online]. Available: `https://www.sciencedirect.com/science/article/pii/B9780128030585000035`.

[54] C. A. Ross and M. A. Poirier, "Protein aggregation and neurodegenerative disease," *Nature Medicine*, vol. 10, no. S7, S10–S17, Jul. 2004. DOI: `10.1038/nm1066`. [Online]. Available: `https://doi.org/10.1038/nm1066`.

[55] N. A. Jessen, A. S. F. Munk, I. Lundgaard, and M. Nedergaard, "The glymphatic system: A beginner's guide," *Neurochemical Research*, vol. 40, no. 12, pp. 2583–2599, May 2015. DOI: `10.1007/s11064-015-1581-6`. [Online]. Available: `https://doi.org/10.1007/s11064-015-1581-6`.

[56] M. A. Biot, "General theory of three-dimensional consolidation," *Journal of applied physics*, vol. 12.2, 1941.

[57] M. Bai, D. Elsworth, and J.-C. Roegiers, "Multiporosity/multipermeability approach to the simulation of naturally fractured reservoirs," *Water Resources Research*, vol. 29.6, pp. 1621–1633, 1993.

[58] E. C. Aifantis, "Introducing a multi-porous medium," *Dev. Mech.*, vol. 9, pp. 209–211, 1993.

[59] R. Oyarzúa and R. Ruiz-Baier, "Locking-free finite element methods for poroelasticity," *SIAM Journal on Numerical Analysis*, vol. 54, no. 5, pp. 2951–2973, Jan. 2016. DOI: `10.1137/15m1050082`. [Online]. Available: `https://doi.org/10.1137/15m1050082`.

[60] J. J. Lee, E. Piersanti, K.-A. Mardal, and M. E. Rognes, *A mixed finite element method for nearly incompressible multiple-network poroelasticity*, 2018. arXiv: `1804.07568 [math.NA]`.

[61] A. H.-D. Cheng and D. T. Cheng, "Heritage and early history of the boundary element method," *Engineering Analysis with Boundary Elements*, vol. 29, no. 3, pp. 268–302, 2005, ISSN: 0955-7997. DOI: `https://doi.org/10.1016/j.enganabound.2004.12.001`. [Online]. Available: `https://www.sciencedirect.com/science/article/pii/S0955799705000020`.

[62] H. P. Langtangen and K.-A. Mardal, *Introduction to Numerical Methods for Variational Problems*. Jan. 2019, ISBN: 978-3-030-23787-5. DOI: `10.1007/978-3-030-23788-2`.

[63] M. Kuchta, K.-A. Mardal, and M. Mortensen, "On the singular neumann problem in linear elasticity," *Numerical Linear Algebra with Applications*, vol. 26, Sep. 2016. DOI: `10.1002/nla.2212`.

[64] P. Bochev and R. Lehoucq, "On the finite element solution of the pure neumann problem," *SIAM Review*, vol. 47, Oct. 2002. DOI: `10.1137/S0036144503426074`.

[65] D. A. Feinberg and A. S. Mark, "Human brain motion and cerebrospinal fluid circulation demonstrated with mr velocity imaging.," *Radiology*, vol. 163, no. 3, pp. 793–799, 1987, PMID: 3575734. DOI: `10.1148/radiology.163.3.3575734`. eprint: `https://doi.org/10.1148/radiology.163.3.3575734`. [Online]. Available: `https://doi.org/10.1148/radiology.163.3.3575734`.

[66] P. K. Eide, "Comparison of simultaneous continuous intracranial pressure (ICP) signals from ICP sensors placed within the brain parenchyma and the epidural space," *Medical Engineering & Physics*, vol. 30, no. 1, pp. 34–40, Jan. 2008. DOI: `10.1016/j.medengphy.2007.01.005`. [Online]. Available: `https://doi.org/10.1016/j.medengphy.2007.01.005`.

[67] P. K. Eide and T. Sæhle, "Is ventriculomegaly in idiopathic normal pressure hydrocephalus associated with a transmantle gradient in pulsatile intracranial pressure?" *Acta Neurochirurgica*, vol. 152, no. 6, pp. 989–995, Feb. 2010. DOI: `10.1007/s00701-010-0605-x`. [Online]. Available: `https://doi.org/10.1007/s00701-010-0605-x`.

[68] V. Vinje, A. Eklund, K.-A. Mardal, M. E. Rognes, and K.-H. Støverud, "Intracranial pressure elevation alters CSF clearance pathways," *Fluids and Barriers of the CNS*, vol. 17, no. 1, Apr. 2020. DOI: 10.1186/s12987-020-00189-1. [Online]. Available: https://doi.org/10.1186/s12987-020-00189-1.

[69] L. Rangel-Castillo, S. Gopinath, and C. S. Robertson, "Management of intracranial hypertension," *Neurologic Clinics*, vol. 26, no. 2, pp. 521–541, May 2008. DOI: 10.1016/j.ncl.2008.02.003. [Online]. Available: https://doi.org/10.1016/j.ncl.2008.02.003.

[70] J. E. Tooke and S. A. Williams, "Capillary blood pressure," in *Continuous Transcutaneous Monitoring*, Springer US, 1987, pp. 209–214. DOI: 10.1007/978-1-4613-1927-6_37. [Online]. Available: https://doi.org/10.1007/978-1-4613-1927-6_37.

[71] D. Greitz, R. Wirestam, A. Franck, B. Nordell, C. Thomsen, and F. Ståhlberg, "Pulsatile brain movement and associated hydrodynamics studied by magnetic resonance phase imaging," *Neuroradiology*, vol. 34, no. 5, pp. 370–380, 1992. DOI: 10.1007/bf00596493. [Online]. Available: https://doi.org/10.1007/bf00596493.

[72] E. Eliseussen, M. E. Rognes, and T. B. Thompson, *A-posteriori error estimation and adaptivity for multiple-network poroelasticity*, 2021. arXiv: 2111.13456 [math.NA].

[73] F. Eskandari, Z. Rahmani, and M. Shafieian, "The effect of large deformation on poisson's ratio of brain white matter: An experimental study," *Proceedings of the Institution of Mechanical Engineers, Part H: Journal of Engineering in Medicine*, vol. 235, no. 4, pp. 401–407, Dec. 2020. DOI: 10.1177/0954411920984027. [Online]. Available: https://doi.org/10.1177/0954411920984027.

[74] K. E. Holter, B. Kehlet, A. Devor, T. J. Sejnowski, A. M. Dale, S. W. Omholt, O. P. Ottersen, E. A. Nagelhus, K.-A. Mardal, and K. H. Pettersen, "Interstitial solute transport in 3d reconstructed neuropil occurs by diffusion rather than bulk flow," *Proceedings of the National Academy of Sciences*, vol. 114, no. 37, pp. 9894–9899, Aug. 2017. DOI: 10.1073/pnas.1706942114. [Online]. Available: https://doi.org/10.1073/pnas.1706942114.

[75] W. Zhan, F. R. y Baena, and D. Dini, "Effect of tissue permeability and drug diffusion anisotropy on convection-enhanced delivery," *Drug Delivery*, vol. 26, no. 1, pp. 773–781, Jan. 2019. DOI: 10.1080/10717544.2019.1639844. [Online]. Available: https://doi.org/10.1080/10717544.2019.1639844.

[76] S.-P. Lee, T. Q. Duong, G. Yang, C. Iadecola, and S.-G. Kim, "Relative changes of cerebral arterial and venous blood volumes during increased cerebral blood flow: Implications for BOLD fMRI," *Magnetic Resonance in Medicine*, vol. 45, no. 5, pp. 791–800, 2001. DOI: `10.1002/mrm.1107`. [Online]. Available: `https://doi.org/10.1002/mrm.1107`.

[77] H. Ito, I. Kanno, H. Iida, J. Hatazawa, E. Shimosegawa, H. Tamura, and T. Okudera, "Arterial fraction of cerebral blood volume in humans measured by positron emission tomography," *Annals of Nuclear Medicine*, vol. 15, no. 2, pp. 111–116, Apr. 2001. DOI: `10.1007/bf02988600`. [Online]. Available: `https://doi.org/10.1007/bf02988600`.

[78] L. Ballerini, T. Booth, M. del C. Valdés Hernández, S. Wiseman, R. Lovreglio, S. Muñoz Maniega, Z. Morris, A. Pattie, J. Corley, A. Gow, M. E. Bastin, I. J. Deary, and J. Wardlaw, "Computational quantification of brain perivascular space morphologies: Associations with vascular risk factors and white matter hyperintensities. a study in the lothian birth cohort 1936," *NeuroImage: Clinical*, vol. 25, p. 102 120, 2020, ISSN: 2213-1582. DOI: `https://doi.org/10.1016/j.nicl.2019.102120`. [Online]. Available: `https://www.sciencedirect.com/science/article/pii/S221315821930467X`.

[79] L. Xie, H. Kang, Q. Xu, M. J. Chen, Y. Liao, M. Thiyagarajan, J. O'Donnell, D. J. Christensen, C. Nicholson, J. J. Iliff, T. Takano, R. Deane, and M. Nedergaard, "Sleep drives metabolite clearance from the adult brain," *Science*, vol. 342, no. 6156, pp. 373–377, Oct. 2013. DOI: `10.1126/science.1241224`. [Online]. Available: `https://doi.org/10.1126/science.1241224`.

[80] A. Mehrabian and Y. N. Abousleiman, "Generalized biot's theory and mandel's problem of multiple-porosity and multiple-permeability poroelasticity," *Journal of Geophysical Research: Solid Earth*, vol. 119, no. 4, pp. 2745–2763, Apr. 2014. DOI: `10.1002/2013jb010602`. [Online]. Available: `https://doi.org/10.1002/2013jb010602`.

[81] K. Heffer, "Theory of linear poroelasticity with applications to geomechanics and hydrogeology," *Journal of Petroleum Science and Engineering*, vol. 45, no. 3-4, pp. 291–292, Dec. 2004. DOI: `10.1016/j.petrol.2004.06.001`. [Online]. Available: `https://doi.org/10.1016/j.petrol.2004.06.001`.

[82] J. H. Smith and J. A. Humphrey, "Interstitial transport and transvascular fluid exchange during infusion into brain and tumor tissue," *Microvascular Research*, vol. 73, no. 1, pp. 58–73, Jan. 2007. DOI: `10.1016/j.mvr.2006.07.001`. [Online]. Available: `https://doi.org/10.1016/j.mvr.2006.07.001`.

[83] V. Libertiaux, F. Pascon, and S. Cescotto, "Experimental verification of brain tissue incompressibility using digital image correlation," *Journal of the Mechanical Behavior of Biomedical Materials*, vol. 4, no. 7, pp. 1177–

1185, 2011, ISSN: 1751-6161. DOI: https://doi.org/10.1016/j.jmbbm.2011.03.028. [Online]. Available: https://www.sciencedirect.com/science/article/pii/S1751616111000737.

[84] J. Berryman and J. Res, "Effective stress for transport properties of inhomogeneous porous rock," *Journal of Geophysical Research*, vol. 97, May 1995. DOI: 10.1029/92JB01593.

[85] J. Berryman and H. Wang, "The elastic coefficients of double-porosity models for fluid transport in jointed rock," *Journal of Geophysical Research Atmospheres*, vol. 100, Jul. 1995. DOI: 10.1029/95JB02161.

[86] I. Sobey and B. Wirth, "Effect of non-linear permeability in a spherically symmetric model of hydrocephalus," *Mathematical Medicine and Biology: A Journal of the IMA*, vol. 23, no. 4, pp. 339–361, Dec. 2006. DOI: 10.1093/imammb/dql015. [Online]. Available: https://doi.org/10.1093/imammb/dql015.

[87] C. F. Rothe, "Reflex control of veins and vascular capacitance," *Physiological Reviews*, vol. 63, no. 4, pp. 1281–1342, Oct. 1983. DOI: 10.1152/physrev.1983.63.4.1281. [Online]. Available: https://doi.org/10.1152/physrev.1983.63.4.1281.

[88] R. Hainsworth, "The importance of vascular capacitance in cardiovascular control," *Physiology*, vol. 5, no. 6, pp. 250–254, Dec. 1990. DOI: 10.1152/physiologyonline.1990.5.6.250. [Online]. Available: https://doi.org/10.1152/physiologyonline.1990.5.6.250.

[89] D. Levine, "The pathogenesis of normal pressure hydrocephalus: A theoretical analysis," *Bulletin of Mathematical Biology*, vol. 61, no. 5, pp. 875–916, Sep. 1999. DOI: 10.1006/bulm.1999.0116. [Online]. Available: https://doi.org/10.1006/bulm.1999.0116.

[90] X. Li, H. von Holst, and S. Kleiven, "Influences of brain tissue poroelastic constants on intracranial pressure (ICP) during constant-rate infusion," *Computer Methods in Biomechanics and Biomedical Engineering*, vol. 16, no. 12, pp. 1330–1343, Dec. 2013. DOI: 10.1080/10255842.2012.670853. [Online]. Available: https://doi.org/10.1080/10255842.2012.670853.

[91] S. Gelman, D. S. Warner, and M. A. Warner, "Venous Function and Central Venous Pressure: A Physiologic Story," *Anesthesiology*, vol. 108, no. 4, pp. 735–748, Apr. 2008, ISSN: 0003-3022. DOI: 10.1097/ALN.0b013e3181672607. eprint: https://pubs.asahq.org/anesthesiology/article-pdf/108/4/735/367607/0000542-200804000-00026.pdf. [Online]. Available: https://doi.org/10.1097/ALN.0b013e3181672607.

[92] C. E. Hagan, B. Bolon, and C. D. Keene, "20 - nervous system," in *Comparative Anatomy and Histology*, P. M. Treuting and S. M. Dintzis, Eds., San Diego: Academic Press, 2012, pp. 339–394, ISBN: 978-0-12-381361-9. DOI: https://doi.org/10.1016/B978-0-12-381361-9.00020-2. [On-

line]. Available: `https://www.sciencedirect.com/science/article/pii/B9780123813619000202`.

[93] G. Kayalioglu, "Chapter 3 - the vertebral column and spinal meninges," in *The Spinal Cord*, C. Watson, G. Paxinos, and G. Kayalioglu, Eds., San Diego: Academic Press, 2009, pp. 17–36, ISBN: 978-0-12-374247-6. DOI: `https://doi.org/10.1016/B978-0-12-374247-6.50007-9`. [Online]. Available: `https://www.sciencedirect.com/science/article/pii/B9780123742476500079`.

[94] H. Ozawa, T. Matsumoto, T. Ohashi, M. Sato, and S. Kokubun, "Mechanical properties and function of the spinal pia mater," *Journal of Neurosurgery: Spine*, vol. 1, no. 1, pp. 122–127, Jul. 2004. DOI: `10.3171/spi.2004.1.1.0122`. [Online]. Available: `https://doi.org/10.3171/spi.2004.1.1.0122`.

[95] A. SMILLIE, I. SOBEY, and Z. MOLNAR, "A hydroelastic model of hydrocephalus," *Journal of Fluid Mechanics*, vol. 539, no. -1, p. 417, Sep. 2005. DOI: `10.1017/s0022112005005707`. [Online]. Available: `https://doi.org/10.1017/s0022112005005707`.

[96] A. Ern and S. Meunier, "A posteriori error analysis of euler-galerkin approximations to coupled elliptic-parabolic problems," *ESAIM: Mathematical Modelling and Numerical Analysis*, vol. 43, no. 2, pp. 353–375, Dec. 2008. DOI: `10.1051/m2an:2008048`. [Online]. Available: `https://doi.org/10.1051/m2an:2008048`.

[97] T. I. Józsa, R. M. Padmos, W. K. El-Bouri, A. G. Hoekstra, and S. J. Payne, "On the sensitivity analysis of porous finite element models for cerebral perfusion estimation," *Annals of Biomedical Engineering*, vol. 49, no. 12, pp. 3647–3665, Jun. 2021. DOI: `10.1007/s10439-021-02808-w`. [Online]. Available: `https://doi.org/10.1007/s10439-021-02808-w`.

[98] S. Garnotel, S. Salmon, and O. Balédent, "Numerical cerebrospinal system modeling in fluid-structure interaction," in *Intracranial Pressure & Neuromonitoring XVI*, T. Heldt, Ed., Cham: Springer International Publishing, 2018, pp. 255–259, ISBN: 978-3-319-65798-1.

[99] B. Fischl, M. I. Sereno, and A. M. Dale, "Cortical surface-based analysis," *NeuroImage*, vol. 9, no. 2, pp. 195–207, Feb. 1999. DOI: `10.1006/nimg.1998.0396`. [Online]. Available: `https://doi.org/10.1006/nimg.1998.0396`.

[100] M. Unnerbäck, J. T. Ottesen, and P. Reinstrup, "ICP curve morphology and intracranial flow-volume changes: A simultaneous ICP and cine phase contrast MRI study in humans," *Acta Neurochirurgica*, vol. 160, no. 2, pp. 219–224, Dec. 2017. DOI: `10.1007/s00701-017-3435-2`. [Online]. Available: `https://doi.org/10.1007/s00701-017-3435-2`.

[101] E. Carrera, D.-J. Kim, G. Castellani, C. Zweifel, Z. Czosnyka, M. Kasprowicz, P. Smielewski, J. D. Pickard, and M. Czosnyka, "What shapes pulse amplitude of intracranial pressure?" *Journal of Neurotrauma*, vol. 27, no. 2, pp. 317–324, Feb. 2010. DOI: 10.1089/neu.2009.0951. [Online]. Available: https://doi.org/10.1089/neu.2009.0951.

[102] J. J. Sloots, G. J. Biessels, and J. J. Zwanenburg, "Cardiac and respiration-induced brain deformations in humans quantified with high-field MRI," *NeuroImage*, vol. 210, p. 116 581, Apr. 2020. DOI: 10.1016/j.neuroimage.2020.116581. [Online]. Available: https://doi.org/10.1016/j.neuroimage.2020.116581.

[103] C. Nicholson, "Diffusion and related transport mechanisms in brain tissue," *Reports on Progress in Physics*, vol. 64, no. 7, pp. 815–884, Jun. 2001. DOI: 10.1088/0034-4885/64/7/202. [Online]. Available: https://doi.org/10.1088/0034-4885/64/7/202.

[104] N. Abbott, "Evidence for bulk flow of brain interstitial fluid: Significance for physiology and pathology," *Neurochemistry International*, vol. 45, no. 4, pp. 545–552, Sep. 2004. DOI: 10.1016/j.neuint.2003.11.006. [Online]. Available: https://doi.org/10.1016/j.neuint.2003.11.006.

[105] M. P. Lun, E. S. Monuki, and M. K. Lehtinen, "Development and functions of the choroid plexus–cerebrospinal fluid system," *Nature Reviews Neuroscience*, vol. 16, no. 8, pp. 445–457, Jul. 2015. DOI: 10.1038/nrn3921. [Online]. Available: https://doi.org/10.1038/nrn3921.

[106] P. K. Eide, L. M. Valnes, E. K. Lindstrøm, K.-A. Mardal, and G. Ringstad, "Direction and magnitude of cerebrospinal fluid flow vary substantially across central nervous system diseases," *Fluids and Barriers of the CNS*, vol. 18, no. 1, Apr. 2021. DOI: 10.1186/s12987-021-00251-6. [Online]. Available: https://doi.org/10.1186/s12987-021-00251-6.